Research paper

Aeroelastic analysis of wind turbine under diverse inflow conditions

Yang Huang [a,c], Xiaolong Yang [b], Weiwen Zhao [a], Decheng Wan [a,*]

[a] *Computational Marine Hydrodynamics Lab (CMHL), School of Naval Architecture, Ocean and Civil Engineering, Shanghai Jiao Tong University, Shanghai, China*
[b] *Offshore Oil Engineering Co. Ltd., Tianjin, China*
[c] *Department of Naval Architecture, Ocean and Marine Engineering, University of Strathclyde, Glasgow, G4 0LZ, UK*

ABSTRACT

As wind turbine blades increase in size and flexibility, the structural deformation becomes more pronounced and significantly influences the aerodynamic performance of the wind turbine. This paper introduces a fluid-structure interaction (FSI) analysis model that employs the actuator line technique and equivalent beam theory to assess the aeroelastic behaviour of wind turbines under various inflow scenarios. After validating the FSI model, it is used to simulate the aeroelastic responses of the NREL 5 MW wind turbine under various inflow conditions. The aerodynamic loads, structural dynamic responses, and wake field characteristics are thoroughly analysed, detailing the effects of various inflow conditions, such as wind speed and inflow type, on the aeroelasticity of the wind turbine. The findings reveal that blade deformation reduces average aerodynamic loads under various inflow conditions, with the effect intensifying at higher wind speeds. Blade deformation's impact is more profound on aerodynamic thrust than on aerodynamic power, and it significantly influences the variation amplitude of aerodynamic loads rather than their average values. Additionally, with increasing wind speed, blade deformation notably increases wake velocity and reduces wake field turbulence intensity. Under turbulent inflow, however, the rise in wake velocity due to blade deformation diminishes, while turbulence intensity increases, comparing with uniform and shear inflow conditions.

1. Introduction

In response to the growing energy crisis and heightened environmental pollution concerns, the wind power industry has witnessed significant growth over the past decades, establishing itself as a cornerstone in the renewable energy landscape. To enhance the economic viability of wind energy, there is a notable trend towards increasing rotor diameter (Musial et al., 2018). Concurrently, there is a shift towards lightweight turbine designs to achieve cost efficiency (Thomas and Ramachandra, 2018). As a result, wind turbine blades have become more slender, lightweight, and flexible (Bošnjaković et al., 2022; Micallef and Rezaeiha, 2021; Enevoldsen and Xydis, 2019). When subjected to wind forces, the blades undergo significant deformation, profoundly affecting the aerodynamic performance of the wind turbine and, by extension, its wake dynamics. Such aerodynamic disturbances, in return, significantly impact the structural stability and safety of the blades (Della Posta et al., 2022; Sayed et al., 2019a, 2019b). This intricate interplay between aerodynamic behaviour and structural dynamics complicates the accurate prediction of the wind turbine's aeroelastic response. Furthermore,

the inflow conditions, characterized by altitude-dependent wind speeds and turbulent flows typical of real-world settings, further amplify blade instability and the complexity of aeroelastic responses (Guma et al., 2021; Li et al., 2020). To guarantee the consistent, efficient, and safe operation of wind turbines, it is essential to delve into the aeroelastic characteristics of rotor blades under various inflow scenarios.

The study of wind turbine aeroelasticity begins with an examination of aerodynamics. Extensive research has been conducted on the aerodynamic characteristics of wind turbines, utilizing a variety of analytical approaches. Among them, the blade element momentum theory (BEMT) stands as a traditional tool. Its inherent simplicity, computational efficiency, and credible accuracy have led to its incorporation into predictive platforms like QBlade (Alaskari et al., 2019), HAWC2 (Larsen et al., 2005), and FAST (Jonkman and Buhl Jr, 2005). Despite the BEMT facing challenges with complex flow conditions, the BEMT-based Fluid-Structure Interaction (FSI) model demonstrates considerable accuracy compared to Computational Fluid Dynamics (CFD) across various practically relevant scenarios (Aryan et al., 2023). Additionally, three-dimensional (3D) panel codes (Boorsma et al., 2022; Greco and

---

* Corresponding author.
  E-mail address: dcwan@sjtu.edu.cn (D. Wan).

Testa, 2021) offer a relatively rapid and precise means to predict aerodynamic characteristics under potential flow conditions, especially for complex three-dimensional shapes. This capability renders them particularly suitable for integration with structural dynamics solvers. To enhance computational precision under challenging flow conditions, such as asymmetric inflow scenarios, the vortex lattice method (VLM), augmented with the vortex core model, has been utilized (Konstadinopoulos et al., 1985). While VLM effectively captures wake structures, its reliance on empirical formulations for distant wake predictions may result in discrepancies. In contrast, CFD provides detailed flow information at blade interfaces and comprehensive 3D wake visualizations by solving the Navier-Stokes equations (Shourangiz-Haghighi et al., 2020). As high-performance computational methodologies advance, CFD is increasingly utilized for high-fidelity wind turbine aerodynamic simulations (Cai et al., 2016; Tran and Kim, 2016a; Lei et al., 2017; Liu et al., 2016), though it requires significant resources. To reduce computational resource demand, integrative models that combine CFD with BEMT have been developed (Mikkelsen, 2003; Sørensen and Shen, 2002; Shen et al., 2007). Specifically, the actuator line model (ALM) uses virtual actuator lines to simulate blades, effectively modelling the 3D wake dynamics. Despite the ALM exhibiting limitations in accurately modelling blade tip flows, necessitating corrections to enhance its model accuracy, its streamlined approach offers computational economy, solidifying its position in numerous wake field investigations (Zheng et al., 2023; Ning and Wan, 2019; Duan et al., 2018; Ai et al., 2017).

Structural simulation is essential for wind turbine aeroelastic predictions. Predominantly, the 3D Finite Element Method (FEM) and the one-dimensional (1D) equivalent beam model (EBM) are utilized (Hansen et al., 2006). While the 3D FEM provides a deeper understanding of structural dynamic responses, especially in blades with complex multi-layer composites, it demands extensive computation resources (Wang et al., 2016). Due to this complexity, rotor blades are usually modelled as equivalent beams for structural assessments. Within the EBM framework, modal approach, multi-body dynamics (MBD), and 1D FEM are standard discretization strategies (Shabana, 2020; Borg et al., 2014). The integration of aerodynamic and structural models has led to the development of several comprehensive aeroelastic frameworks (Calabretta et al., 2016; Qu et al., 2018; Jeong et al., 2014a; Dai et al., 2017; Meng et al., 2018; Ma et al., 2019; Hsu and Bazilevs, 2012; Li et al., 2015). Calabretta et al. (2016) developed an aeroelastic model using a modal approach and a nonlinear beam model to study the aeroelastic behaviour of wind turbine blades. Similarly, Qu et al. (2018) formulated an analytical model employing a similar method to analyse nonlinear vibrations in blades of floating offshore wind turbines (FOWTs). Jeong et al. (2014a) investigated aeroelastic behaviours in shear and turbulent flows using BEMT and the free-wake method. Dai et al. (2017) applied Unsteady Reynolds Averaged Navier-Stokes (URANS) and 3D FEM to examine blade aeroelasticity at different yaw angles. Meng et al. (2018) investigated wake interactions among wind turbines using ALM and 1D EBM. Ma et al. (2019) developed ALFMEM, an aeroelastic analysis tool focusing on wake dynamics influenced by aeroelastic behaviours, integrating ALM and FEM. Hsu and Bazilevs (2012) introduced a comprehensive FSI methodology for wind turbine simulations, integrating CFD for aerodynamics and 1D FEM for structural responses. Moreover, Li et al. (2015) combined CFD and MBD to explore the aeroelastic intricacies of wind turbines.

While several coupled models have been developed to analyse the aeroelastic performance of wind turbines (Zheng et al., 2023; Ponta et al., 2016; Gebhardt and Roccia, 2014; Yu and Kwon, 2014), those based on potential flow theory exhibit limited accuracy in complex inflow scenarios, particularly in wake interactions among multiple turbines. In contrast, the CFD approach, although highly detailed, requires substantial computational resources. The ALM provides a balanced solution by offering relatively accurate predictions of aerodynamic loads and wake characteristics while significantly reducing computational demands. However, existing ALM-based aeroelastic models fail to account for blade torsional deformation. This study aims to address and refine this limitation. Furthermore, there has been scant research on how blade deformation influences wake field characteristics.

In the present work, an FSI analysis model integrating ALM and EBM is proposed to investigate the aeroelastic behaviour of wind turbines under diverse inflow conditions. An improved ALM predicts aerodynamic loads considering blade deformations, while the EBM, based on Euler-Bernoulli beam theory, calculates structural deformations using two-node elements with six degrees of freedom, covering flap-wise, edgewise, and torsional deformations for a detailed structural dynamics analysis. A two-way coupling strategy effectively links the fluid and structural analyses. Implemented with large eddy simulation (LES), this model allows for comprehensive assessments of the NNREL 5 MW wind turbine's aeroelastic performance under varying wind speeds and inflow types. The aerodynamic loads, blade-root-bending moments, blade-tip displacements, and wake field characteristics are thoroughly examined to investigate the influence of blade deformation on the aeroelastic performance of wind turbine.

This paper is structured as follows: Section 2 introduces the proposed aeroelastic model. Section 3 details the computational setup for the simulations. Section 4 presents validation results and simulation outcomes of the wind turbine's aeroelastic responses to various inflow conditions. Section 5 discusses the impact of blade deformation on aeroelastic performance. The conclusions are summarized in the final section.

2. FSI analysis model

2.1. Aerodynamic model

To minimize the computational demands of resolving boundary layer flows near wind turbine blades, this study employs the ALM, developed by Sørensen and Shen (2002), for aerodynamic performance predictions. In the ALM, blades are modelled as virtual actuator lines, subdivided into discrete actuator points that simulate airfoil sections. Aerodynamic forces are represented by body forces at these actuator points, calculated from bidimensional airfoil data and localized inflow parameters. The body forces are then projected into the flow field to reflect the influence of the blades on the flow, thereby enabling the modelling of the turbine's three-dimensional vortex and wake development. Although the ALM delivers precise aerodynamic predictions for wind turbine, it does not account for the structural deformations of blades. Modifications to the original ALM are necessary to include the effects of velocity and positional variations resulting from blade deformation.

To clarify the vector relationship of speeds and forces in aeroelastic calculations, coordinate systems are illustrated in Fig. 1(a). Each blade operates in a unique rotating coordinate system: Direction 2 aligns with the blade's spanwise direction, and Direction 1 corresponds to the blade's rotational direction. Additionally, the vector in Direction 0 is derived from the cross product of vectors in Directions 2 and 1. Fig. 1(c) displays the speed vectors for an airfoil section of the blade.

$$\boldsymbol{U}_{\text{rel}} = \boldsymbol{U}_{\text{in}} + \boldsymbol{U}_{\text{b}} + \boldsymbol{U}_{\text{s}} \tag{1}$$

$$\boldsymbol{U}_{\text{b}} = \boldsymbol{\Omega} \times \boldsymbol{r} \tag{2}$$

where $\boldsymbol{U}_{\text{rel}}$ is the relative wind speed vector at the blade section, comprising the vector sum of local wind speed vector $\boldsymbol{U}_{\text{in}}$, rotating speed vector $\boldsymbol{U}_{\text{b}}$, and the structural vibration speed $\boldsymbol{U}_{\text{S}}$ induced by blade deformation, $\boldsymbol{\Omega}$ is the angular speed of rotor, $\boldsymbol{r}$ denotes the distance vector from the hub to the actuator point's position. It is noted that $\boldsymbol{U}_{\text{in}}$ is not the inflow wind speed at the inlet boundary but the flow field velocity at the actuator points, obtained through linear interpolation of the flow field velocities at the mesh points (Lee et al., 2016).
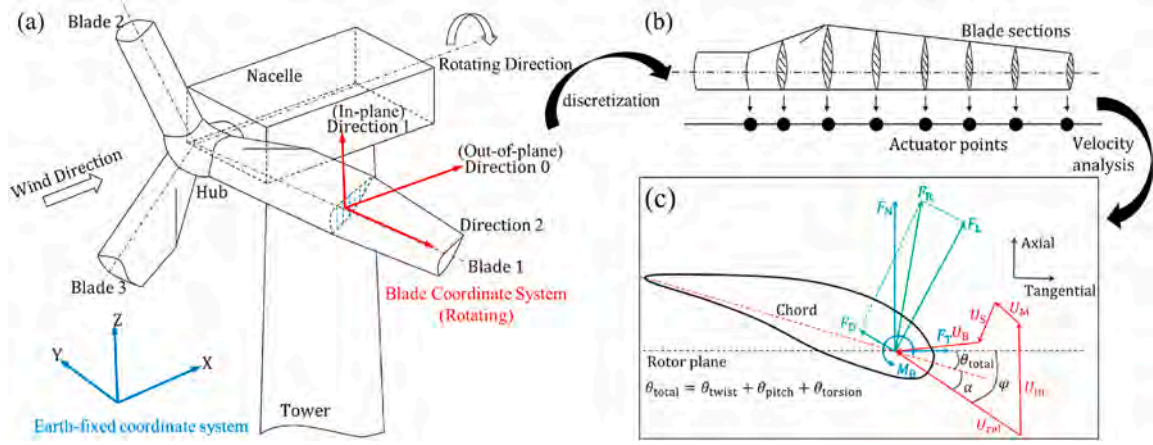
Fig. 1. Schematic diagram of modified actuator line model: (a) Definition of different coordinate systems; (b) Discretization of wind turbine blades; (c) Speed vectors of an airfoil section.

The local angle of attack (AOA) α can be obtained using following equations:

$$\alpha = \varphi - \theta_t \tag{3}$$

$$\varphi = \arctan(U_0 / U_1) \tag{4}$$

$$\theta_t = \theta_p + \theta_w + \theta_s \tag{5}$$

where φ is local inflow angle, U_0 and U_1 are velocity components of $\boldsymbol{U}_{rel}$ projected to the blade coordinate system, θ_p, θ_w, and θ_s represent the blade pitch angle, local twist angle, and structural torsional angle induced by blade deformation, respectively.

Furthermore, the lift and drag coefficients at the blade cross-section can be obtained by interpolating the AOA in the blade aerodynamic database. Then, the aerodynamic forces are determined by:

$$\boldsymbol{f} = (\boldsymbol{L}, \boldsymbol{D}) = \frac{1}{2}\rho_a |\boldsymbol{U}_{rel}|^2 (C_L \boldsymbol{e}_L + C_D \boldsymbol{e}_D)c\mathrm{d}r \tag{6}$$

where $\boldsymbol{L}$ and $\boldsymbol{D}$ are lift and drag force vectors, respectively, C_L and C_D represent lift and drag coefficients, respectively, ρ_a denotes the air density, c is chord length, $\mathrm{d}r$ is width of airfoil segment, $\boldsymbol{e}_L$ and $\boldsymbol{e}_D$ stand for the unit vectors of lift and drag forces, respectively.

The body force $\boldsymbol{f}$ is the vector summation of the forces exerted on each actuator point, which is further modified by Glauert's tip loss correction to more accurately reflect the impact of the tip vortices on blade performance (Shen et al., 2005). These body forces are then integrated into the flow field through the regularization kernel function η_ε:

$$\eta_\varepsilon(d) = \frac{1}{\varepsilon^3 \pi^{3/2}} exp\left[-\left(\frac{d}{\varepsilon}\right)^2\right] \tag{7}$$

$$\boldsymbol{f}_\varepsilon(x,y,z,t) = \boldsymbol{f} \otimes \eta_\varepsilon = \sum_{i=1}^{N} \boldsymbol{f}(x_i,y_i,z_i,t)\frac{1}{\varepsilon^3 \pi^{3/2}} exp\left[-\left(\frac{d_i}{\varepsilon}\right)^2\right] \tag{8}$$

As presented in Eq. (8), the aerodynamic force $\boldsymbol{f}_\varepsilon(x,y,z,t)$ generated by the wind turbine at (x,y,z,t) is the sum of the projected components of all body forces here, where N denotes the number of actuator points, with i signifying the index of a specific actuator point, d_i indicates the separation between a position (x,y,z) in flow field and the location of ith actuator point, and ε is employed to adjust the projection width of the body force. Based on the previous study conducted by Sørensen et al. (1998), a recommend value for ε is twice of the grid side length and therefore ε is set to 4.0 in the present simulation.

The governing equations of transient and viscous airflow are derived from Navier-Stocks equations. To effectively capture the multi-scale vortex dynamics and turbulence distribution within the turbine wake,

this study employs the LES approach. Accordingly, the flow governing equations are formulated as follows:

$$\frac{\partial \overline{u_i}}{\partial \overline{x_i}} = 0 \tag{9}$$

$$\rho\frac{\partial \overline{u_i}}{\partial t} + \rho\frac{\partial(\overline{u_i}\,\overline{u_j})}{\partial \overline{x_j}} = -\frac{\partial p}{\partial x_i} + \frac{\partial}{\partial x_j}\left[\mu\left(\frac{\partial \overline{u_i}}{\partial \overline{x_j}} + \frac{\partial \overline{u_j}}{\partial \overline{x_i}}\right)\right] + \frac{\partial \tau_{ij}^s}{\partial x_j} + f_\varepsilon \tag{10}$$

where $\overline{u}$ represents the filtered velocity vector field. p denotes the pressure field. μ is the kinematic viscosity. $\tau_{ij}^s = -\rho(\overline{u_i u_j} - \overline{u_i}\,\overline{u_j})$ represents the subgrid-scale (SGS) Reynolds stress in LES, which is dealt with by the standard Smargorinsky eddy viscosity model (Ning and Wan, 2019) in the simulation. f_ε is the source term calculated from the improved ALM.

2.2. Structural model

Owing to their slender design, large wind turbine blades can be effectively modelled as cantilever beams in structural analysis. An equivalent beam model based on Euler-Bernoulli beam theory is employed to calculate the structural deformation of wind turbine blades. The equivalent beam model is discretized using a two-node beam element with six degrees-of-freedom (DOF). At each node, three deformation types, including flap-wise deformation (δ_0) along x_2-axis, edge-wise deformation (δ_1) along y_2-axis, and torsional deformation (δ_θ) around z_2-axis, are considered. Fig. 2 illustrates the dynamic equilibrium analysis for a representative blade element within the structural model. There are three types of forces considered in the structural analysis: aerodynamic loads, which include aerodynamic force ($\boldsymbol{F}_a$) and aerodynamic torque ($\boldsymbol{M}_a$), gravity force ($\boldsymbol{G}$), and centrifugal force ($\boldsymbol{N}_r$). It is noted that the spin-softening effect, induced by the centrifugal force, is also taken into account.

The structural dynamics equations based on the principle of virtual work are chosen as the governing equations to predict the dynamic responses of wind turbine blades. These equations are discretized by the FEM and are represented as MCK equations.

$$[M]\ddot{\boldsymbol{x}} + [C]\dot{\boldsymbol{x}} + [K]\boldsymbol{x} = \boldsymbol{F} \tag{11}$$

$$\boldsymbol{x} = \begin{bmatrix} \boldsymbol{x}_0 & \boldsymbol{x}_1 & \boldsymbol{x}_\theta \end{bmatrix}^T \tag{12}$$

where $[M]$ represents the total mass matrix, $[C]$ is the damping matrix, $[K]$ denotes the total stiffness matrix, $\boldsymbol{F}$ is the external force vector, $\boldsymbol{x}$ is the displacement vector, including the displacement along the flap-wise direction $\boldsymbol{x}_0$, the displacement along the edgewise direction $\boldsymbol{x}_1$, and the angular displacement $\boldsymbol{x}_\theta$. To determine the damping matrix $[C]$,
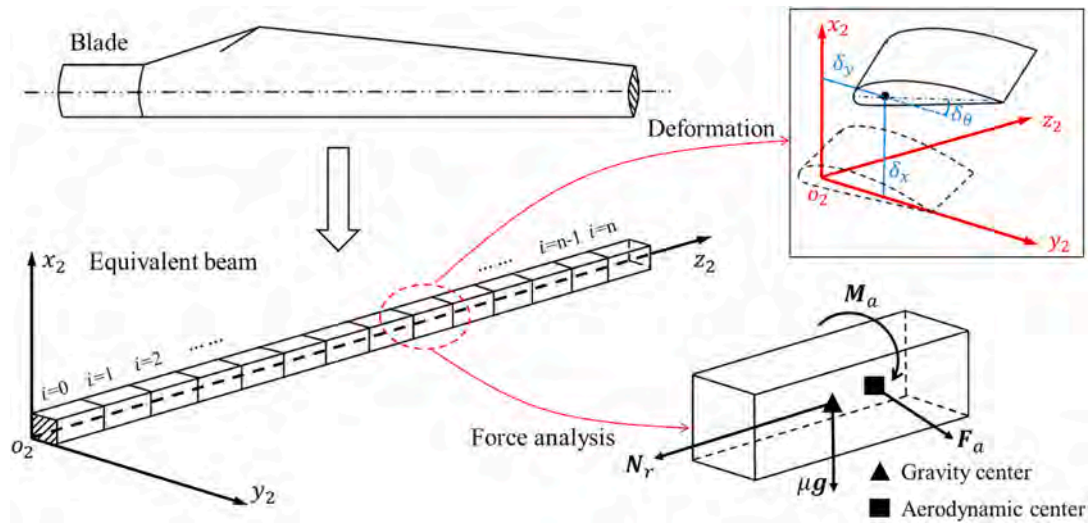
Fig. 2. Dynamic equilibrium analysis for a typical blade element in structural model.

Rayleigh damping is introduced in the structural model. The damping matrix is assembled according to the damping ratio ξ, the first and second natural frequencies of the blade (f_{n1}, f_{n2}).

$$[C] = \alpha[M] + \beta[K] \tag{13}$$

$$\begin{bmatrix} \alpha \\ \beta \end{bmatrix} = \frac{2\xi}{f_{n1} + f_{n2}} \begin{bmatrix} 2\pi f_{n1}f_{n2} \\ 1/2\pi \end{bmatrix} \tag{14}$$

2.3. Fluid-structuring coupling

The aerodynamic and structural models are integrated through a two-way coupling strategy, formulating a FSI model for the flexible blades of wind turbines. As depicted in Fig. 3, the calculation of structural deformation incorporates the effects of aerodynamic forces. Moreover, the alterations in position and additional velocity due to blade deformation are accounted for during aerodynamic force computations. It should be noted that this FSI model is grounded in a weak coupling approach, which is more efficient than a strong coupling strategy. When determining the aerodynamic loads for the subsequent time step, the blade deformation from the current step is factored in. This model is developed as a C++ class based on OpenFOAM (Jasak et al., 2007). Additionally, this class is embedded to the pimpleFoam solver within OpenFOAM to facilitate aeroelastic simulations of wind turbines.

3. Computational set up

3.1. Physical model

In this study, the NREL 5 MW wind turbine is selected as the subject of analysis, a model that has been extensively investigated (Dose et al., 2018; Yu et al., 2018; Chow and Van Dam, 2012). The rotor diameter is 126 m. The rated wind speed for the wind turbine is 11.4 m/s, and the corresponding rotor speed is 12.1 RPM (Revolutions Per Minute). More detailed specifications of this wind turbine including structural properties can be found in References (Jonkman et al., 2009; Bazilevs et al., 2011). As indicated by Fig. 4, the wind blade blades are discretized into a series of actuator points in the present aerodynamic model.
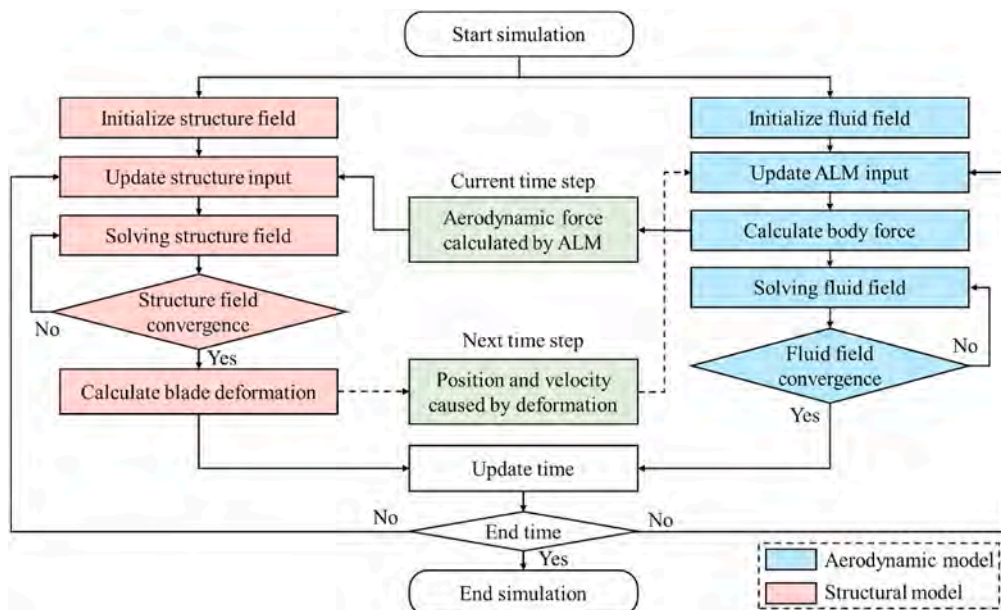
Fig. 3. Solving procedure of the coupled aeroelastic model.
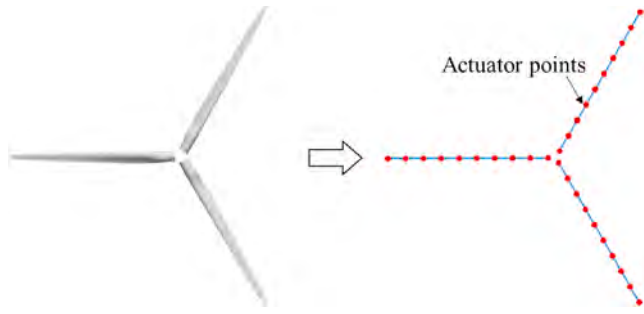
Fig. 4. Schematic diagram of NREL 5 MW wind turbine using actuator line model.

Additionally, the simulation emphasizes the modelling of the wind turbine blades, excluding the nacelle and tower components. It is noted that the title angle of main shaft and pre-cone angle of the wind turbine blade are considered in the numerical simulation.

3.2. Computational domain

A computational domain with dimensions of 2020 m (x) × 630 m (y) × 470 m (z) is established. The wind turbine is positioned at the centre of the domain, $3D$ (where $D = 126$ m represents the rotor diameter) away from the inlet boundary. To capture the fully developed turbine wake, a wake region extending $13D$ in length is incorporated. Furthermore, to account for the wake's expansion, the gap between the blade tip and the top boundary is set at $2.5D$. Fig. 5 provides a detailed depiction of the computational domain. To balance computational accuracy and efficiency, various mesh resolutions are utilized throughout the domain. As depicted in Fig. 6, the turbine wake region features a finer mesh to effectively capture detailed wake dynamics. Near the wind turbine blades, the grid has a side length of 2 m, while the surrounding background mesh adopts an 8 m grid size.

The boundary conditions are defined as follows: the inlet boundary velocity is determined by the inflow wind conditions. The outlet boundary is assigned to a zero-gradient condition. The top and bottom boundaries are both treated as free-slip surfaces. The sidewalls employ symmetric conditions.

3.3. Inflow condition

Three distinct inflow scenarios, uniform, shear, and turbulent, are examined in this study. For the uniform inflow scenario, three different inflow wind speeds (u_{in}) are considered. To achieve the optimal tip speed ratio, the rotational speed of the wind turbine varies with different wind speeds, as listed in Table 1. The shear inflow utilizes an exponential model (Dolan and Lehn, 2006; Spera, 1994) to represent the height-dependent wind speed. The magnitude of the wind speed (u_z) at a given height (z) is defined by:
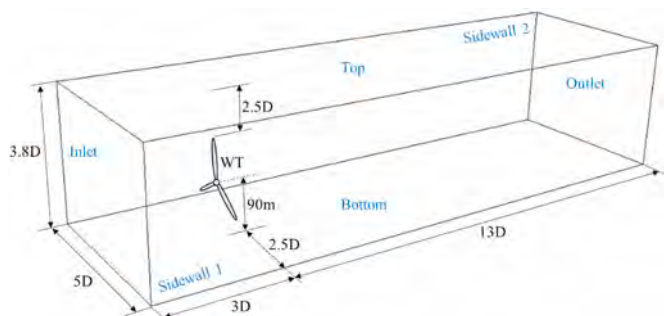
Fig. 5. Schematic diagram of computation domain.

$$u_z = u_0 \left(\frac{z}{H_0} \right)^\alpha \tag{15}$$

where u_0 is wind speed at hub height H_0. For the turbulent inflow scenario, a varying wind speed is chosen. The turbulence intensity (I_T) is defined as:

$$I_T = \frac{\sigma}{\bar{u}} \tag{16}$$

where σ represents the standard deviation, $\bar{u}$ denotes the time-averaged wind speed.

To investigate the impact of blade deformation and inflow condition on the aerodynamic performance of wind turbines, numerical simulations are performed for the NRRL 5 MW wind turbine under varying inflow conditions, both with and without considering blade deformation. All simulation scenarios are summarized in Table 1.

This study conducted all numerical simulations on the Cirrus UK National Tier-2 High-Performance Computing (HPC) Service at EPCC, utilizing Cirrus standard compute nodes. Each node is equipped with two 18-core Intel Xeon E5-2695 (Broadwell) series processors, operating at 2.1 GHz. The simulation time for each case is set to 420 s, and each case utilizes one node. The computational time ranges from 14.7 to 16.4 h per case. Additionally, the computational time per timestep of the present FSI model, incorporating modified ALM and EBM, is compared with the blade-resolved CFD-CSD approach from Yu and Kwon's study (Yu and Kwon, 2014), as detailed in Table 2. The proposed FSI model demonstrates a significant reduction in computational time relative to the blade-resolved CFD-CSD method.

4. Numerical results

This section begins with the validation results of the FSI model, followed by sensitivity analyses related to grid resolution and time step size to identify the optimal computational parameters. The exploration of the aeroelastic behaviour of the wind turbine under uniform inflow across various wind speeds is then presented, concluding with an analysis of the turbine' aeroelastic performance under different inflow conditions.

4.1. FSI model validation

The current FSI model integrates both aerodynamic and structural components. Our previous research has confirmed the reliability of the aerodynamic model employing ALM (Zheng et al., 2023; Ning and Wan, 2019; Ai et al., 2017; Huang et al., 2021). Therefore, the present verification focuses on the structural model and the coupled aeroelastic model.

4.1.1. Structural model
Fig. 7 depicts a cantilever beam simulated using the structural model, initially set with a specific velocity, mirroring the setup described by Khayyer et al. (2018). The initial velocity distribution along the cantilever beam is detailed in Eqs. (17) and (18), and the primary structural parameters of the cantilever beam are summarized in Table 3. The structural simulation employs a time step size of 0.005s and utilizes 40 beam elements. Fig. 8 shows the predicted displacement at the free end of the cantilever beam. In the absence of damping, the displacement exhibits sinusoidal oscillations over time. The deformation predicted by the structural model closely aligns with the theoretical estimate, demonstrating its effectiveness in representing structural deformations.

$$v_y(x) = 0.01 c_0 \frac{f(x)}{f(l)}, c_0 = \sqrt{\frac{K^s}{\rho^s}} \tag{17}$$
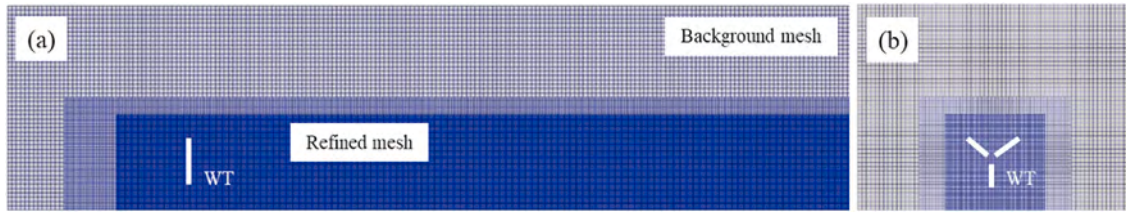
Fig. 6. Grid distribution in computation domain, where 'WT' represents the wind turbine: (a) *xz* plane; (b) *yz* plane.

Table 1
Inflow conditions for aeroelastic modelling of NREL 5 MW wind turbine.

Case	Inflow type	Wind speed (m/s)	Rotor speed (RPM)	Blade deformation
1/2	Uniform	$u_{in} = (11.4, 0, 0)$	12.1	On/Off
3/4	Uniform	$u_{in} = (8, 0, 0)$	9.13	On/Off
5/6	Uniform	$u_{in} = (5, 0, 0)$	7.48	On/Off
7/8	Shear	$u_z = (11.4, 0, 0)$, $\alpha = 0.15$	12.1	On/Off
9/10	Turbulent	$\bar{u} = (11.4, 0, 0)$, $I_T = (0.2, 0.16, 0.16)$	12.1	On/Off

Table 2
Computational time per time step for different FSI methods.

	Grid number (million)	CPU clock speed (GHz)	CPU number	Computational time (s)
Yu and Kwon (Yu and Kwon, 2014)	5.93	2.8	120	12.0
Present	6.62	2.1	36	2.8

$$f(x) = (\cos kl + \cosh kl)(\cosh kx - \cosh kx)$$
$$+ (\sin kl - \sinh kl)(\sinh kx - \sin kx) \qquad (18)$$

Additionally, the natural frequencies of a single blade of the NREL 5 MW wind turbine, absent aerodynamic loads and at zero rotation speed, are calculated using the current structural model. These results are then compared with data obtained from FAST and previous studies (Li et al., 2020; Jeong et al., 2014b), as detailed in Table 4. Furthermore, the effects of rotation and gravity on the structural dynamics of blades are considered. As detailed in Table 5, the first six natural frequencies of a rotating blade at 12.1 RPM are presented and compared with existing literature (Paraskeva, 2018). It is observed that, regardless of blade rotation, resonant agreements are achieved, demonstrating the accuracy and reliability of the current structural model in simulating wind turbine blades.

4.1.2. Aeroelastic model

To validate the accuracy of the current aeroelastic model, numerical simulations are conducted for the NREL 5 MW wind turbine operating under different wind speeds and uniform inflow conditions. The simulation results, including aerodynamic loads and blade

Table 3
Structural parameters of the cantilever beam.

Parameter	Value	Unit
Structural density ρ^s	1×10^3	kg/m^3
Elastic module K^s	3.25×10^6	pa
moment of inertia	6.67×10^{-7}	m^4
Initial velocity of free end	0.01	m/s
Damping coefficient α	0	–
Damping coefficient β	0	–
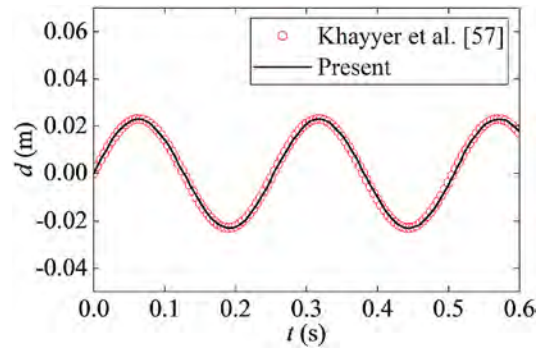
Fig. 8. Time history of the displacement at the free end of cantilever beam.

Table 4
Natural frequencies of a non-rotating blade of the NREL 5 MW wind turbine.

Mode	FAST (Hz)	Jeong et al. (Jeong et al., 2014b) (Hz)	Li et al. (Li et al., 2020) (Hz)	Present (Hz)
f_{n1} (1st flapwise)	0.68	0.67	0.68	0.67
f_{n2} (1st edgewise)	1.10	1.11	1.10	1.10
f_{n3} (2nd flapwise)	1.94	1.93	1.98	1.97
f_{n4} (2nd edgewise)	4.00	3.96	3.99	4.01
f_{n5} (3rd flapwise)	4.43	4.43	4.66	4.67
f_{n6} (1st torsion)	5.77	5.51	5.53	5.73

Fig. 7. Sketch of cantilever beam with initial velocity: (a) Geometry shape; (b) Initial velocity.

Table 5
Natural frequencies of a rotating blade at 12.1 RMP of the NREL 5 MW wind turbine.

Mode	Paraskeva (Paraskeva, 2018)	Present (Hz)
f_{n1} (1st flap-wise)	0.737	0.721
f_{n2} (1st edgewise)	1.150	1.141
f_{n3} (2nd flap-wise)	2.048	2.013
f_{n4} (2nd edgewise)	4.124	4.013
f_{n5} (3rd flap-wise)	4.668	4.785
f_{n6} (1st torsion)	5.592	5.735

deformations, are benchmarked against data from prior studies (Li et al., 2020; Yu and Kwon, 2014; Jonkman et al., 2009; Jeong et al., 2014b; Kim and Kwon, 2019).

The distribution of time-averaged blade deformation along span-wise direction under rated wind speed ($u_{in} = 11.4$ m/s) is depicted in Fig. 9. It is observed that the predicted blade bending deformation (δ_0 and δ_1) and torsional deformation (δ_θ), closely aligns with results from other numerical methods. Additionally, the unsteady aerodynamic load and aeroelastic responses of blade #1 at a wind speed of 8 m/s also show reasonable agreement with the numerical results from Kim and Kwon (Yu and Kwon, 2014), as present in Fig. 10. Furthermore, the mean aerodynamic loads and blade tip deformations at different wind speeds are listed in Table 6. Compared with the data from existing literature, our numerical findings exhibit minimal discrepancies, thereby demonstrating the accuracy of the proposed aeroelastic model.

4.2. Sensitivity analysis of grid size and time step

The grid sensitivity analysis in this study is performed by employing three distinct mesh resolutions, as detailed in Table 7. The medium mesh is configured with dimensions of 2 m × 2 m × 2 m, resulting in a total grid number of 6.62 million. In comparison, the fine mesh's grid number is scaled up to $2\sqrt{2}$ times that of the medium mesh, while the coarse mesh's grid number is reduced to $1/2\sqrt{2}$ times. For the grid convergence test, a time step of 0.02 s is selected, based on findings from a previous study (Ning and Wan, 2019). This specific time step allows the wind turbine blade to rotate approximately $1.5°$ per step, which aligns closely

with recommendations from existing literature (Tran and Kim, 2016b). To evaluate time step sensitivity, three different time steps are analysed: 0.01 s, 0.02 s, and 0.03 s, each in conjunction with the medium mesh. The details of these time steps are outlined in Table 8. All sensitivity tests are carried out under uniform inflow conditions, with a rated wind speed of 11.4 m/s. Additionally, the rotor speed is consistently maintained at 12.1 RPM throughout these tests.

The FSI model is utilized to simulate the aeroelastic responses of the NREL 5 MW wind turbine under three distinct mesh resolutions. Fig. 11 presents the comparison of the root mean square (RMS) values of aerodynamic loads and blade deformation, expressed as percentage differences relative to the results from the fine mesh. The findings indicate that the discrepancies in aerodynamic loads between the fine and medium meshes are minimal. However, a more significant variation is observed when comparing the fine mesh with the coarse mesh. Similarly, the pattern of blade deformation aligns with the trends noted in aerodynamic loads across different grid densities. Specifically, the deviation in all deformations remains below 1.3% when comparing the fine and medium meshes. In contrast, these deviations all escalate to above 3.1% when the fine mesh is compared with the coarse mesh. It suggests that the medium mesh offers reliable accuracy in predicting the aeroelastic responses of the wind turbine.

The results of the time step sensitivity analysis, which examines aerodynamic loads and blade tip movements at varying time steps, are illustrated in Fig. 12. The aeroelastic responses of the wind turbine, encompassing aerodynamic loads and blade tip displacements, exhibit minimal discrepancies when compared between time step sizes of 0.02 s and 0.01 s. The observed differences are less than 1%, indicating that a time step of 0.02 s effectively meets the convergence criteria.

4.3. Aeroelastic responses under various wind speeds

The aeroelastic behaviours of the wind turbine at varying inflow wind speeds (5 m/s, 8 m/s, 11.4 m/s) are examined in this section, focusing on the aerodynamic loads, structural deformation, and wake field characteristics. Additionally, the influence of blade deformation on the aeroelastic responses of the wind turbine is investigated.
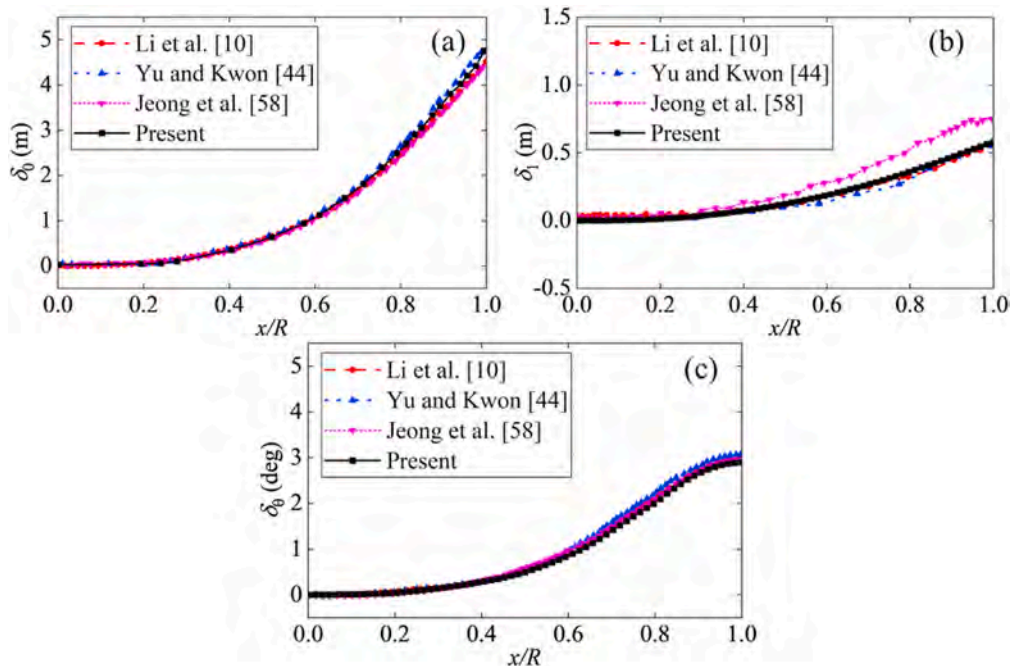
Fig. 9. Time-averaged blade deformation along the span-wise direction under rated wind speed ($u_{in} = 11.4$ m/s): (a) Flap-wise deformation; (b) Edgewise deformation; (c) Torsional deformation ($R = 63$ m is the rotor radius of NREL 5 MW wind turbine).
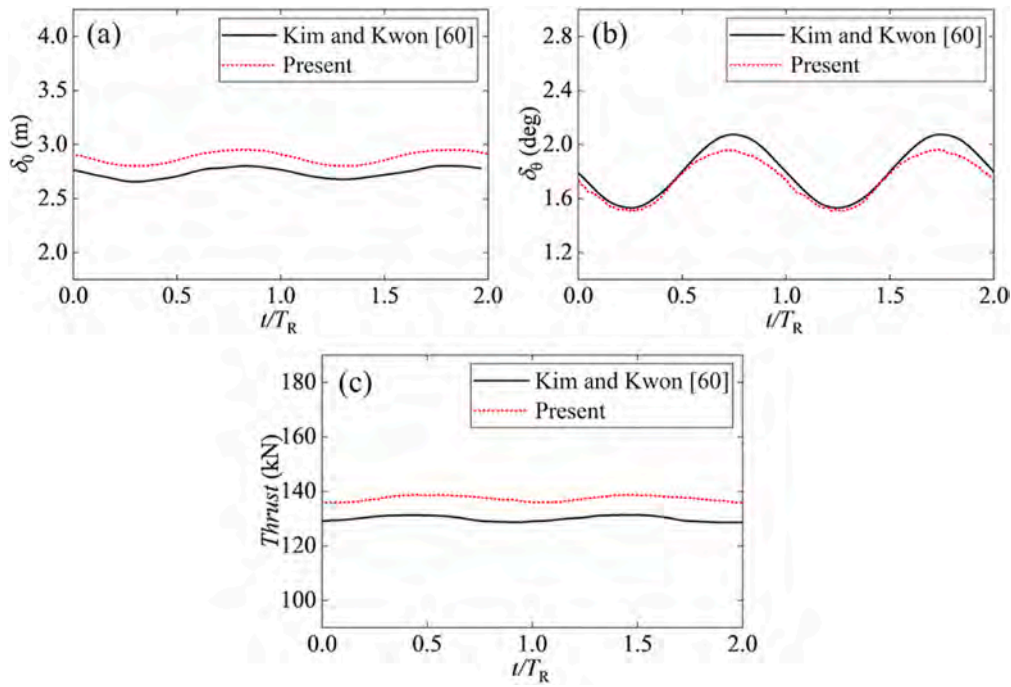
Fig. 10. Aeroelastic responses and aerodynamic load of blade #1 at a wind speed of 8 m/s: (a) Flap-wise deformation δ_0; (b) Torsional deformation δ_θ; (c) Aerodynamic thrust (T_R represents the rotational period of the rotor).

Table 6
Mean aerodynamic loads and blade tip deformations of the NREL 5 MW wind turbine under different wind speeds and uniform inflow condition.

u_{in} (m/s)	No.	Flap-wise deformation (m)	Edgewise deformation (m)	Torsional deformation (deg)	Aerodynamic power (MW)	Aerodynamic thrust (kN)
11.4	Yu and Kwon (Yu and Kwon, 2014)	4.72	0.63	3.06	5.22	656.43
	Li et al. (Li et al., 2020)	4.49	0.57	2.96	5.30	678.44
	Jeong et al. (Jeong et al., 2014b)	4.83	0.75	3.00	–	–
	Present	4.50	0.57	2.96	5.23	658.48
8	Kim and Kwon (Kim and Kwon, 2019)	2.79	–	1.82	1.81	396.40
	Yu and Kwon (Yu and Kwon, 2014)	2.97	–	1.70	1.97	–
	Present	2.88	0.41	1.74	1.89	411.84
5	Kim and Kwon (Kim and Kwon, 2019)	1.57	–	1.16	0.49	180.18
	Yu and Kwon (Yu and Kwon, 2014)	1.63	–	1.06	0.55	–
	Present	1.67	0.33	1.07	0.53	228.74

Table 7
Mesh resolution in grid convergence test.

Case	Description	Side length of grid	Total grid number
g1	Fine mesh	$\sqrt{2}$ m	18.35 million
g2	Medium mesh	2 m	6.62 million
g3	Coarse mesh	$2\sqrt{2}$ m	2.30 million

Table 8
Time step size in sensitivity test.

Case	Description	Time step
t1	Small time step	0.01 s
t2	Medium time step	0.02 s
t3	Large time step	0.03 s

4.3.1. Aerodynamic loads

To better understand the impact of blade deformation on the aerodynamic loads of wind turbines across various wind speeds, the ratios of aerodynamic load coefficients with and without blade deformation are calculated, as outlined in Eq. (19).

$$R_{CP} = C_P/C_P', R_{CT} = C_T/C_T' \tag{19}$$

where C_P and C_T denote the aerodynamic power coefficient and aerodynamic thrust coefficient, respectively, with the prime symbol ' indicating scenarios without considering blade deformation. The outcomes of this comparative analysis are presented in Fig. 13. Observations reveal that with differing inflow wind speeds, incorporating blade deformation results in a reduction of the RMS values of C_P and C_T, with the magnitude of this reduction growing as wind speed increases. This trend underscores the escalating significance of blade deformation on aerodynamic loads with higher wind speeds. Notably, the reduction in RMS values for aerodynamic thrust outstrips that for aerodynamic
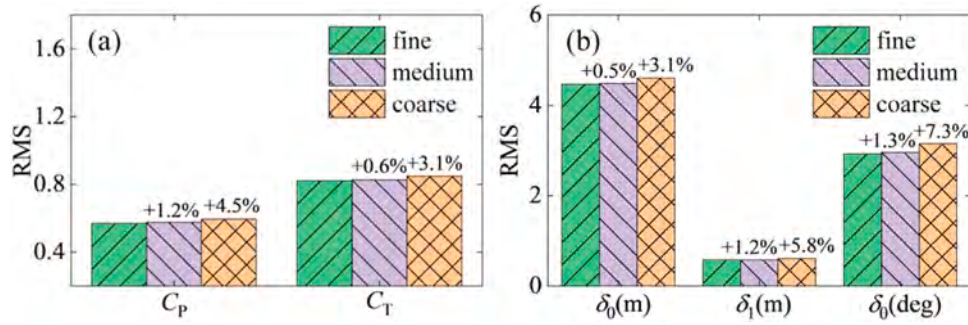
Fig. 11. Comparison of the wind turbine's aeroelastic responses across varied mesh resolutions: (a) Aerodynamic power coefficient (C_P) and aerodynamic thrust coefficient (C_T); (b) Blade tip flap-wise deformation (δ_0), edgewise deformation (δ_1), and torsional deformation (δ_θ).
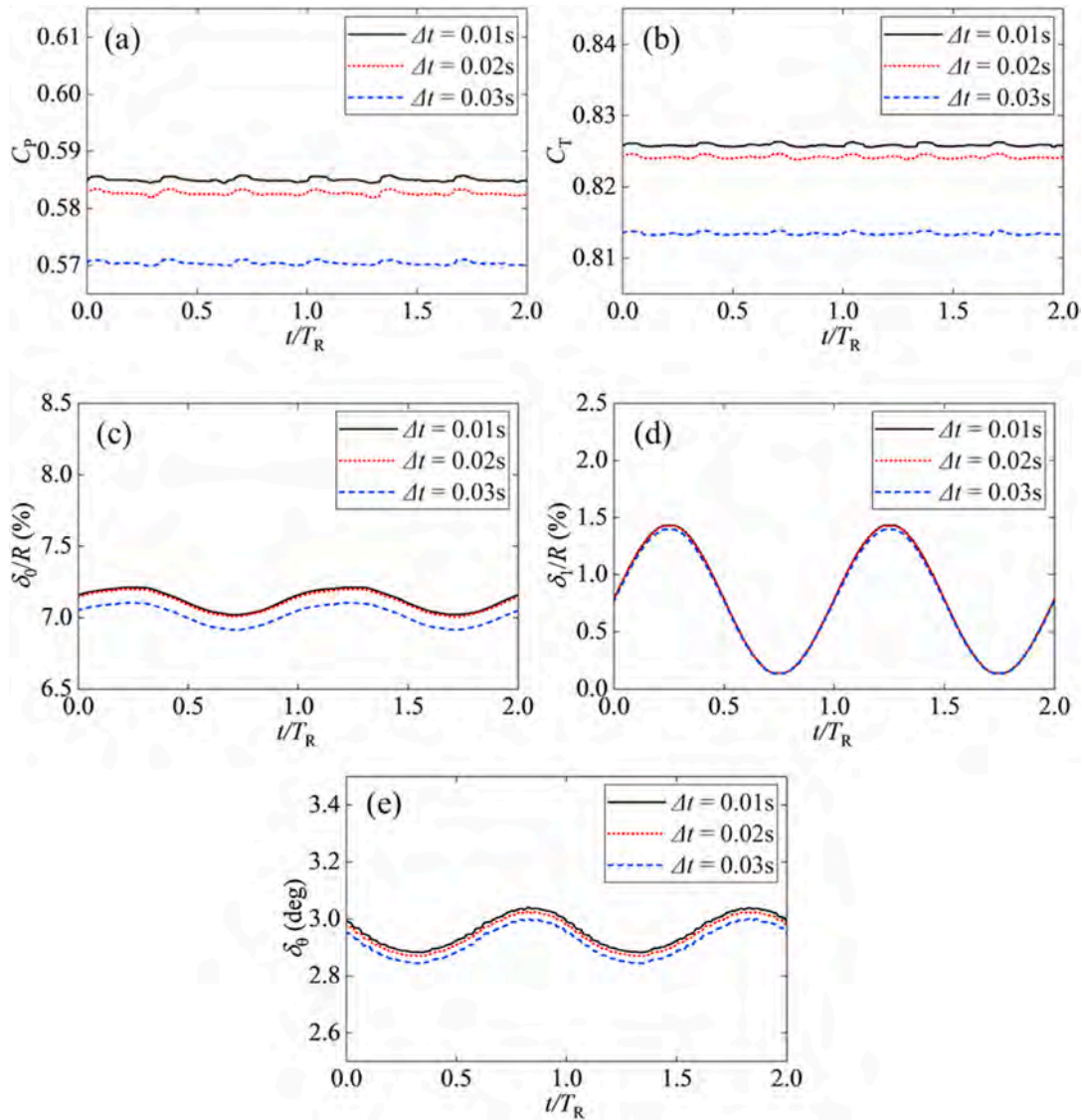
Fig. 12. Temporal trends of the aeroelastic behaviours of wind turbine based on time step variations are shown as: (a) Aerodynamic power coefficient (C_P); (b) Aerodynamic thrust coefficient (C_T); (c) Flap-wise deformation (δ_0) at the blade tip; (d) Edgewise deformation (δ_1) at the blade tip; (f) Torsional deformation (δ_θ) at the blade tip ($T_R = 4.96$s).

power, implying that blade deformation exerts a more substantial influence on aerodynamic thrust.

Moreover, our analysis indicates that the effect of blade deformation on the variation amplitude of aerodynamic load coefficients is contingent upon wind speed. At the low inflow wind speed ($u_{in} = 5$ m/s), blade deformation contributes to a 33% decrease in the standard deviation (STD) of C_P. Conversely, at higher wind speeds ($u_{in} = 8$ m/s and 11.4 m/s), blade deformation incites an increase exceeding 23% in the STD of
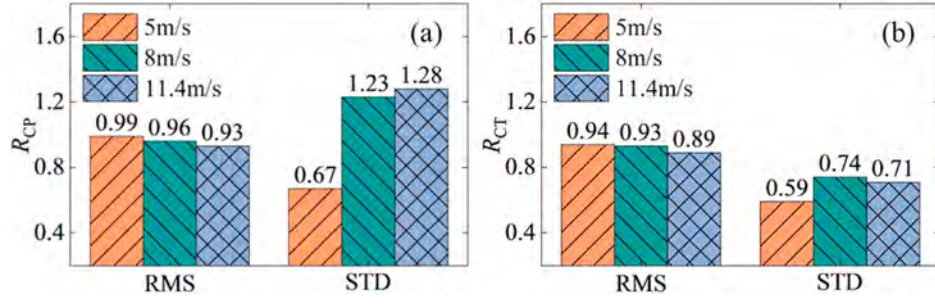
Fig. 13. Comparative analysis of aerodynamic loads on the wind turbine with and without blade deformation across different inflow wind speeds: (a) Aerodynamic power coefficient; (b) Aerodynamic thrust coefficient.

C_P. Across all wind speeds assessed, blade deformation markedly diminishes the STD of C_T, highlighting its profound impact on the stability of aerodynamic thrust.

Here, the reasons behind changes in the aerodynamic loads of the wind turbine caused by blade deformation are further investigated. As indicated by Eq. (6), there are two critical factors affecting aerodynamic responses: the AOA and the magnitude of the relative wind speed (U_{mag}). Figs. 14 and 15 present the temporal and spatial distribution of AOA and U_{mag} for blade #1 under rated wind speed ($u_{in} = 11.4$ m/s). It is observed that considering blade deformation, there is a notable decrease in AOA from the mid-section to the tip of the blade ($0.5 < x/L < 1$), while U_{mag} experiences a slight increase. The reduction in AOA can lead to a decrease in the lift coefficient, thereby reducing aerodynamic loads, whereas the increase in U_{mag} tends to augment aerodynamic loads. Given the significant reduction in wind turbine aerodynamic loads with blade deformation as depicted in Fig. 13, it can be inferred that blade deformation primarily influences the aerodynamic loads of wind turbines by altering the AOA of the blades.

Furthermore, the impact of blade deformation on blade root bending moments at different wind speeds is investigated, including the out-of-plane moment (M_{oop}) and the low-speed-axis moment (M_{lsa}). The ratios of blade root bending moments with and without structural deformation at varying wind speeds are calculated using Eq. (20), and the results are presented in Fig. 16.

$$R_{Moop} = M_{oop}/M_{oop}', \quad R_{Mlsa} = M_{lsa}/M_{lsa}' \tag{20}$$

where the prime symbol ' indicates scenarios excluding blade deformation.

Across three distinct inflow wind speeds, blade deformation results in a notable decrease in both the RMS and the STD of M_{oop} and M_{lsa}. This trend highlights that blade deformation effectively reduces the blade root bending moments, offering a substantial advantage in diminishing the fatigue loads on the blades. Notably, as the inflow wind speed escalates from 5 m/s to 11.4 m/s, the decrease in the RMS of M_{oop} broadens from 7% to 14%, while for M_{lsa}, it enlarges from 1% to 7%. This pattern underscores the amplified impact of blade deformation on

blade root bending moments with an increase in wind speed, particularly highlighting that its effect on M_{lsa} is smaller than on M_{oop}. Moreover, as the wind speed rises, the reduction in the STD of M_{oop} attributed to blade deformation progressively expands from 14% to 40%, in contrast, the reduction in the STD of M_{lsa} contracts from 24% to 7%. This variation signifies that the influence of blade deformation on the STD of M_{oop} and M_{lsa} diverges as wind speed changes.

A deeper examination into the decrease in RMS and STD of blade root bending moments at varying wind speeds due to blade deformation reveals a consistent pattern: the reduction in STD invariably exceeds that in RMS. This observation suggests that blade deformation exerts a more pronounced effect on the variation amplitude of blade root bending moments than on their average magnitude.

4.3.2. Blade deformation

The structural deformation of wind turbine blade #1, including flapwise deformation (δ_0), edgewise deformation (δ_1), and torsional deformation (δ_θ), is examined to investigate the aeroelastic performance of the wind turbine under varying wind speeds. As illustrated in Fig. 17, δ_0, δ_1, and δ_θ all exhibit similar periodic trends, with the period of variation matching the rotor's rotation period. Compared to δ_0, δ_1 has a smaller mean value but significantly larger variations. Such pronounced changes in δ_1 can adversely affect the structural stability and fatigue life of the wind turbine blades. Additionally, it is observed that δ_θ reaches an average of about 3° at rated wind speed, significantly reducing the blade's AOA as indicated by Eqs. (3)–(5), thereby leading to a decrease in aerodynamic loads.

Moreover, the RMS and STD values of blade deformation in different directions across various wind speeds are compared, as illustrated in Fig. 18. With the increase in wind speed, the aerodynamic loads acting on the wind turbine blades rise, leading to an increase in the RMS of all blade deformations, including δ_0, δ_1, and δ_θ. As the inflow wind speed increases from 5 m/s to 11.4 m/s, the RMS values for δ_0 and δ_θ increase by 1.7 times and 1.8 times, respectively, while the RMS for δ_1 increases by 0.8 times. This indicates that, compared to δ_1, δ_0 and δ_θ are more sensitive to changes in wind speed.
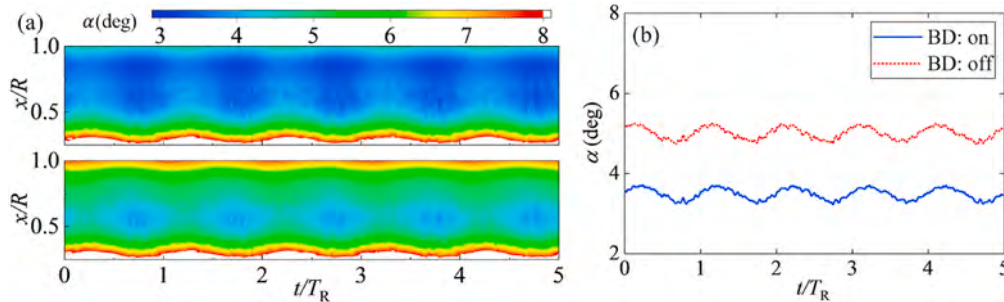
Fig. 14. AOA for wind turbine blade #1 under rated wind speed ($u_{in} = 11.4$ m/s): (a) Temporal and spatial distribution of AOA; (b) Time history of AOA at $x/R = 0.8$, where R is the rotor radius, T_R is the rotational period, and BD signifies "Blade Deformation").
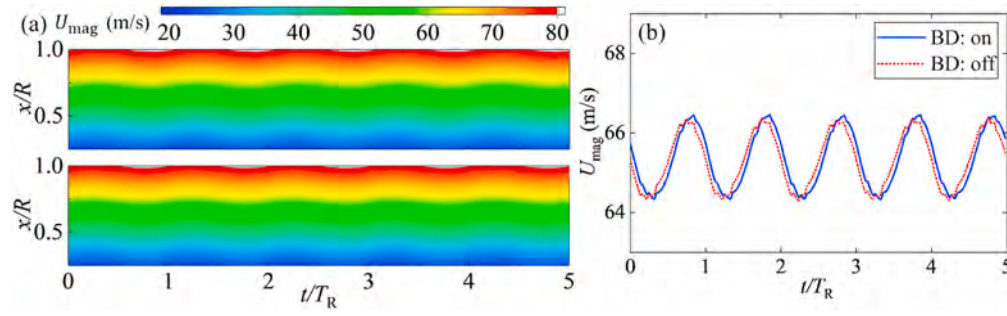
Fig. 15. Magnitude of relative wind speed (U_{mag}) for wind turbine blade #1 under rated wind speed ($u_{in} = 11.4$ m/s): (a) Temporal and spatial distribution of U_{mag}; (b) Time history of U_{mag} at $x/R = 0.8$, where R is the rotor radius, T_R is the rotational period, and BD signifies "Blade Deformation").
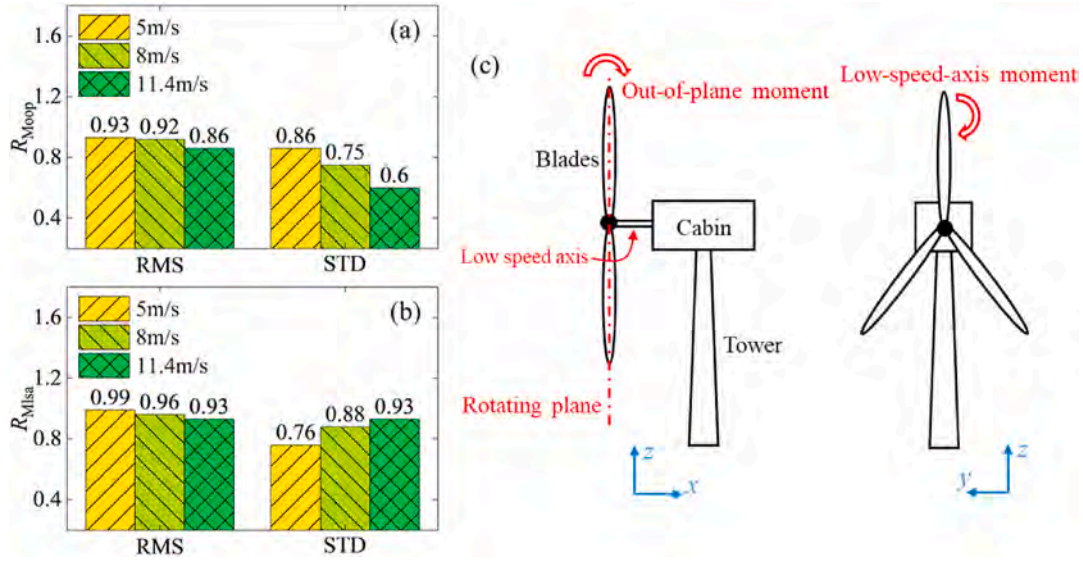
Fig. 16. Comparison results of blade root bending moments of blade #1 with and without blade deformation across different inflow wind speeds: (a) Out-of-plane moment M_{oop}; (b) Low-speed-axis moment M_{lsa}; (c) Schematic diagram of the blade root bending moments.

It is noteworthy that the trend in STD of blade structural deformation in different directions varies with wind speed; the STD of δ_θ significantly increases with wind speed, whereas the STDs of δ_0 and δ_1 decrease as wind speed rises. In terms of variability, the STD of δ_0 is most sensitive to changes in wind speed, followed by δ_0, and then δ_1.

4.3.3. Wake field characteristics

To investigate the impact of blade deformation on the wake characteristics of a wind turbine, the ratios of time-averaged wake velocity (u_w) and turbulence intensity (TI) with and without considering blade deformation are calculated using Eq. (21):

$$R_{uw} = u_w/u_w', R_{TI} = TI/TI' \tag{21}$$

Here, the prime symbol ' indicates scenarios that exclude blade deformation.

As depicted in Fig. 19, the wake velocity distribution at hub-height in the horizontal plane ($z = 90$ m) is presented, with white lines representing the position of the wind turbine and black lines indicating the boundary where $R_{uw} = 1$. It is evident that considering blade deformation results in a significant increase in wake velocity ($R_{uw} > 1$) behind the blades, with a more substantial increase at lower inflow wind speeds than at higher speeds. Moreover, as the inflow wind speed increases, the region exhibiting an increase in wake velocity due to blade deformation gradually extends from $x/D = 4$ to $x/D = 12$.

In terms of turbulence intensity, as shown in Fig. 20, within the near wake region ($x/D < 3$), considering blade deformation leads to an increase in turbulence intensity. However, in the region from $3 < x/D < 6$, blade deformation tends to decrease the turbulence intensity. Beyond $x/D > 6$, the change in turbulence intensity due to blade deformation varies with the inflow wind speed. Specifically, at an inflow wind speed of 5 m/s, blade deformation significantly increases the turbulence intensity in the wake region beyond $x/D > 6$. At a wind speed of 8 m/s, the region of significant turbulence intensity increases shifts to beyond $x/D > 9$, whereas at 11.4 m/s, blade deformation does not enhance turbulence intensity within the wake region between $6 < x/D < 13$. Overall, with the increase in wind speed, the enhancement of wake turbulence intensity resulting from blade deformation becomes increasingly subtle.

As depicted in Fig. 21, the Q-criterion is employed to visualize the vortex structures of the wind turbine at various wind speeds, with the vortex structures coloured by the dimensionless velocity deficit $U_d = (U_{in} - U_w)/U_{in}$. The Q value is calculated by the following equation:

$$Q = \frac{1}{2}\left(\|\boldsymbol{\Omega}\|^2 - \|\boldsymbol{S}\|^2\right) \tag{22}$$

where $\boldsymbol{\Omega}$ represents the rotation tensor, $\boldsymbol{S}$ denotes the strain rate sensor. $\|\boldsymbol{\Omega}\|^2$ quantifies the rotational strength of the flow, while $\|\boldsymbol{S}\|^2$ measures the shear strength.

The helical tip vortices generated by the blade tips are clearly captured, and these vortices gradually dissipate as the wake distance increases. It should be noted that the vortices do not truly "disappear"; rather, the Q values fall below the threshold of 5e-3 used for visualizing the wake structures. This phenomenon can be attributed to the evolution
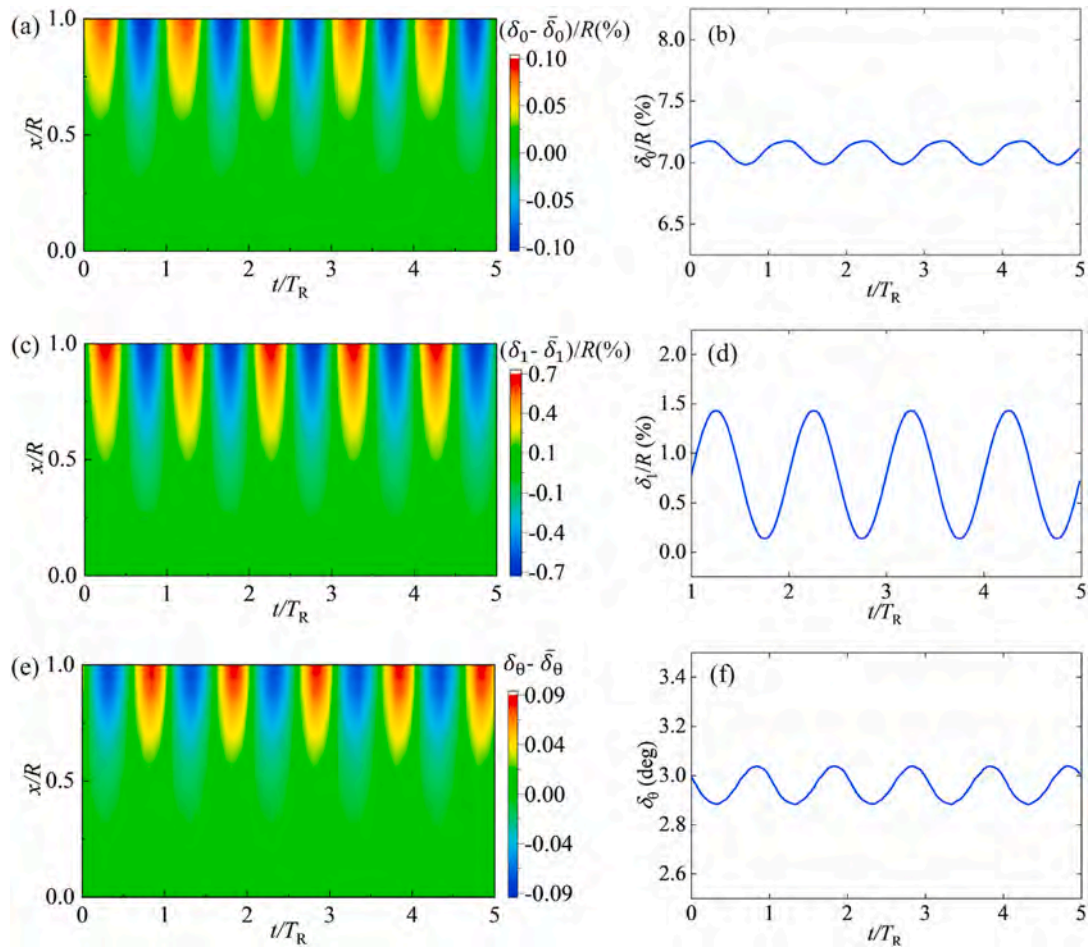
Fig. 17. Structural deformation of wind turbine blade #1 under rated wind speed ($u_{in} = 11.4$ m/s): (a) Time and spatial distribution of δ_0; (b) Time history of δ_0 at the blade tip; (c) Time and spatial distribution of δ_1; (d) Time history of δ_1 at the blade tip; (e) Time and spatial distribution of δ_θ; (b) Time history of δ_θ at the blade tip (R is the rotor radius, T_R is the rotational period).
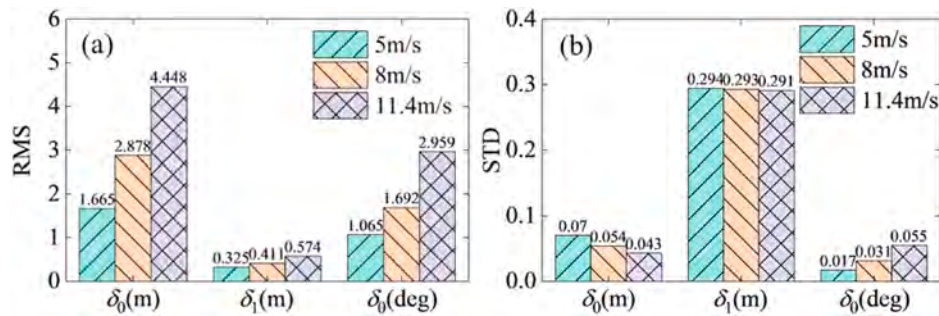
Fig. 18. Blade tip deformation of blade #1 of the wind turbine under varying wind speeds: (a) RMS; (b) STD.

of the wake. In the near wake region, immediately behind the tip vortices, the flow is often chaotic and heavily influenced by strong shear forces due to proximity to the object and immediate wake effects. Therefore, the dominance of the shear component $\|S\|^2$ over the rotational component $\|\Omega\|^2$ leads to reduced Q values, which indicates the "disappearance" of vortex structures. As the flow progresses into the far wake, the influence of shear forces diminishes, allowing the rotational component to regain dominance. Consequently, the Q value increases to above 5e-3, enabling the vortex structures to "reappear". It is observed that blade deformation causes the wake structure to "reappear" at a greater distance in the far wake region, which may be related to the reduction of the rotational strength of the flow due to blade deformation.

4.4. Aeroelastic responses under different inflow types

Compared to uniform inflow conditions, shear and turbulent inflow more closely mirror the actual operating environments of wind turbines. To deepen our understanding of how these different inflow conditions affect the wind turbine's aeroelastic behaviours, this section analyses the turbine's aeroelastic responses to both shear and turbulent inflow conditions.
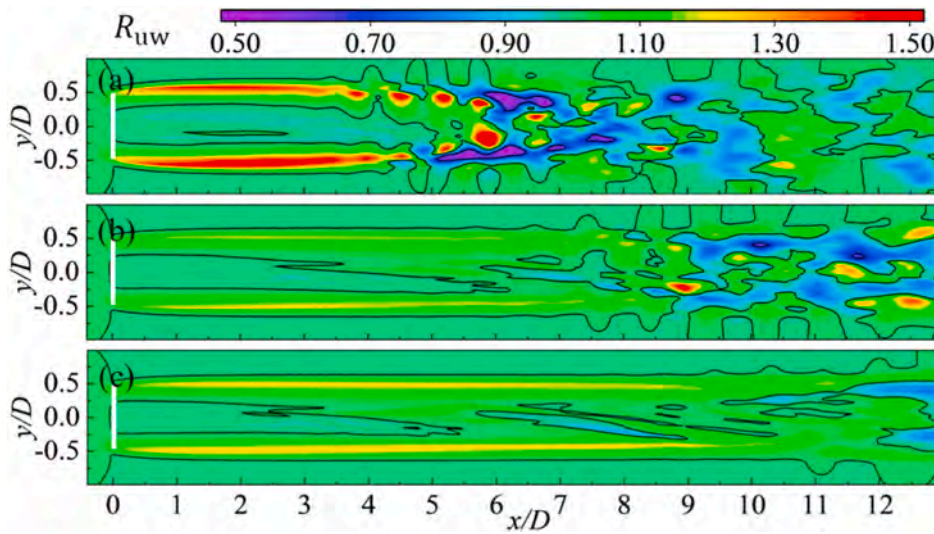
Fig. 19. Comparative analysis of wake velocity in hub-height horizontal plane ($z = 90$ m): (a) $u_{in} = 5$ m/s; (b) $u_{in} = 8$ m/s; (c) $u_{in} = 11.4$ m/s (White line indicates the wind turbine's position).
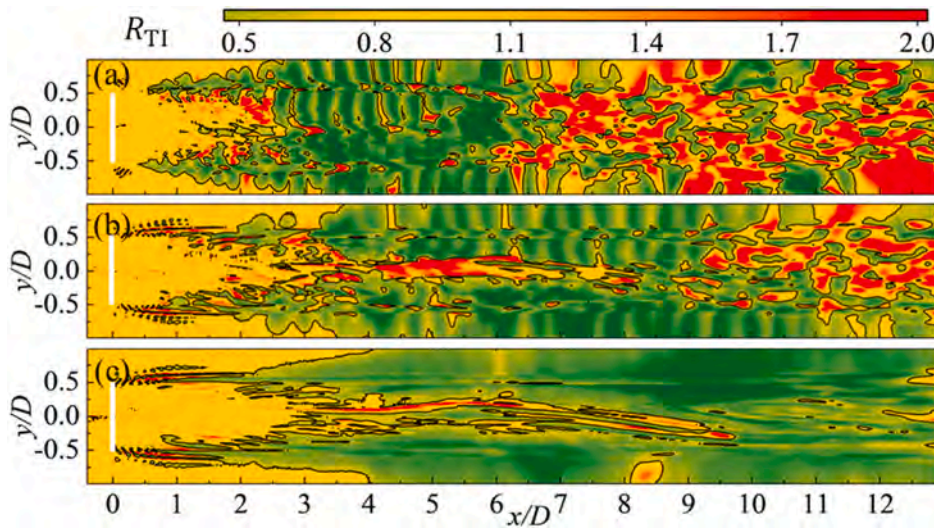
Fig. 20. Comparative analysis of turbulence intensity in hub-height horizontal plane ($z = 90$ m): (a) $u_{in} = 5$ m/s; (b) $u_{in} = 8$ m/s; (c) $u_{in} = 11.4$ m/s (White line indicates the wind turbine's position).

4.4.1. Aerodynamic loads

To visually compare different inflow conditions, the instantaneous inflow velocity distribution at a cross-section ($x = -50$ m) upstream of the wind turbine position is plotted, as shown in Fig. 22. Compared to uniform inflow, shear inflow significantly increases the variability of wind speed across the span of the rotor, while turbulent inflow notably enhances the non-uniformity of velocities across the rotor disk. These variations in inflow conditions can significantly affect the aerodynamic loads on the wind turbine. The RMS and STD values of aerodynamic load coefficients are summarized in Table 9. It can be seen that compared to uniform inflow, under shear and turbulent inflow conditions, the STD of aerodynamic loads increases significantly, regardless of whether blade deformation is considered. This means that the instability in the wind turbine's power output and structural response is heightened, which adversely impacts the performance of the wind turbine.

The ratios of aerodynamic load coefficients, with and without considering blade deformation, are calculated using Eq. (19) and shown in Fig. 23 to explore the effect of blade deformation on aerodynamic loads across different inflow types. Under different inflow types, blade

deformation consistently reduces the RMS of both C_P and C_T, with the reduction in C_T being greater than in C_P. Interestingly, the reduction in RMS for C_P is 7% across all inflow conditions, while for C_P, it is 11%, indicating that the impact of blade deformation on the mean aerodynamic loads is relatively consistent across different inflow types. In contrast to the RMS, the effect of blade deformation on the STD of aerodynamic loads varies significantly with the type of inflow. Under uniform inflow, blade deformation increases the STD of C_P but decreases the STD of C_T. However, under shear and turbulent inflow conditions, blade deformation leads to a notable decrease in the STD for both C_P and C_T, especially under shear inflow, where the STD of C_P and C_T decreases by 53% and 31%, respectively.

Table 10 presents a comprehensive comparison of the RMS and STD of blade root bending moments across various inflow conditions, considering both scenarios with and without blade deformation. Notably, under shear or turbulent inflow, the RMS values of blade root bending moments show minimal variation compared to uniform inflow, irrespective of blade deformation. However, a significant increase in STD is observed, particularly under shear inflow conditions. This
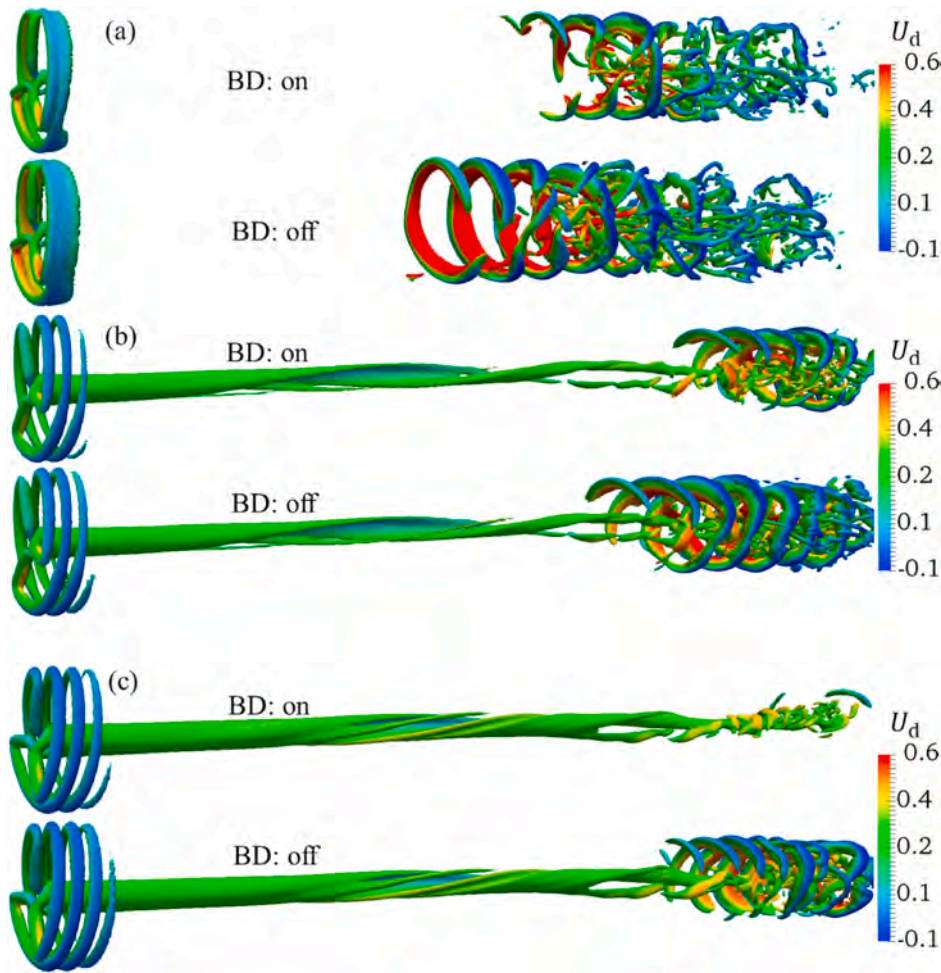
Fig. 21. Vortex structures ($Q = 5e\text{-}3$) of the wind turbine under varying wind speeds: (a) $u_{in} = 5$ m/s; (b) $u_{in} = 8$ m/s; (c) $u_{in} = 11.4$ m/s (BD signifies "Blade Deformation").
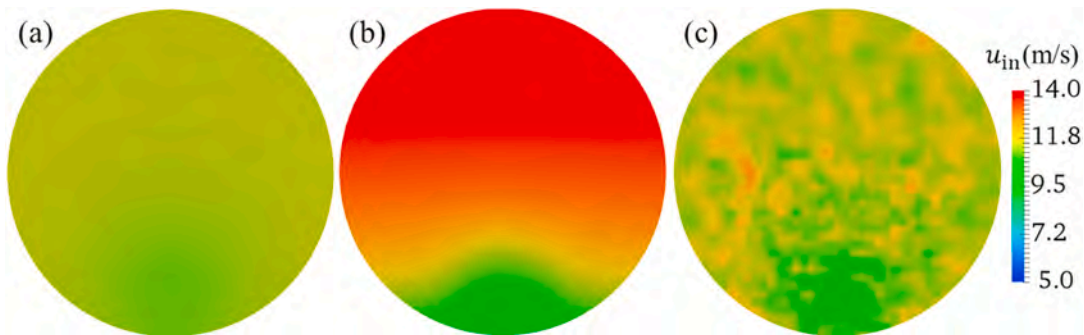
Fig. 22. Instantaneous inflow velocity at the cross-section ($x = -50$ m) upstream of the wind turbine under different inflow conditions: (a) Uniform inflow; (b) Shear inflow; (c) Turbulent inflow.

pronounced rise in STD can be attributed to the considerable variations in inflow wind speed, as depicted in Fig. 22.

Additionally, the ratios of blade root bending moments with and against scenarios without blade deformation are elevated using Eq. (20), with findings illustrated in Fig. 24. Across the different inflow conditions analysed, blade deformation led to a reduction in the RMS values of M_{oop} and M_{lsa} by 14% and 7%, respectively. This indicates a more pronounced impact of blade deformation on M_{oop}. The influence of blade deformation on the RMS of blade root bending moments exhibits minimal variance across inflow types. In contrast, the effect of blade deformation on the STD of blade root bending moments is contingent upon the

specific inflow condition. Under turbulent inflow, blade deformation contributes to a decrease in the STD of M_{oop} and M_{lsa} by 28% and 16%, respectively. Conversely, in shear inflow conditions, the reductions are modest, at only 2% and 3%, respectively. This highlights that blade deformation's impact on the STD of blade root bending moments is relatively minor under shear inflow, as opposed to its more significant influence under uniform and turbulent inflow conditions.

4.4.2. Blade deformation

The blade tip deformation of wind turbine blade #1 under various inflow types is depicted in Fig. 25. Across different inflow types,

Table 9

Aerodynamic load coefficient of the wind turbine under different inflow types.

Inflow condition	Blade deformation	Aerodynamic power coefficient C_P		Aerodynamic thrust coefficient C_T	
		RMS	STD	RMS	STD
Uniform	On	0.518	2.93e-4	0.743	1.83e-4
	Off	0.555	2.29e-4	0.835	2.58e-4
Shear	On	0.511	4.13e-4	0.737	3.72e-4
	Off	0.547	8.76e-4	0.830	5.42e-4
Turbulent	On	0.522	6.63e-3	0.745	5.18e-3
	Off	0.559	8.28e-3	0.838	5.85e-3
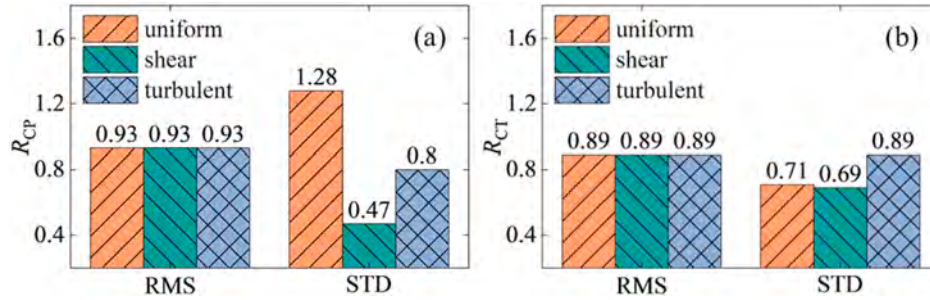
Fig. 23. Comparative analysis of aerodynamic loads on the wind turbine with and without blade deformation under different inflow conditions: (a) Aerodynamic power coefficient; (b) Aerodynamic thrust coefficient.

Table 10

Blade root bending moment of blade #1 of the wind turbine under different inflow types.

Inflow condition	Blade deformation	Out-of-plane bending moment M_{oop} (kNm)		Low-speed-axis bending moment M_{lsa} (kNm)	
		RMS	STD	RMS	STD
Uniform	On	8212	76	1275	15
	Off	9508	128	1367	16
Shear	On	8156	374	1264	124
	Off	9445	382	1352	128
Turbulent	On	8240	118	1286	39
	Off	9533	163	1378	47

deformations in various directions exhibit similar periodic trends, with the period of change corresponding to the rotor's rotation period. Comparing the time history curves of blade deformation in different directions, it is observed that, across various inflow types, the most significant variation occurs in flap-wise deformation δ_0, while edgewise deformation δ_1 and torsional deformation δ_θ are minimally affected by the inflow type. As shown in Fig. 26, under different inflow types, the RMS of δ_θ varies by less than 2%. Compared to uniform inflow, under shear inflow and turbulent inflow conditions, the STD values of δ_θ increase by 4 times and 0.83 times, respectively.
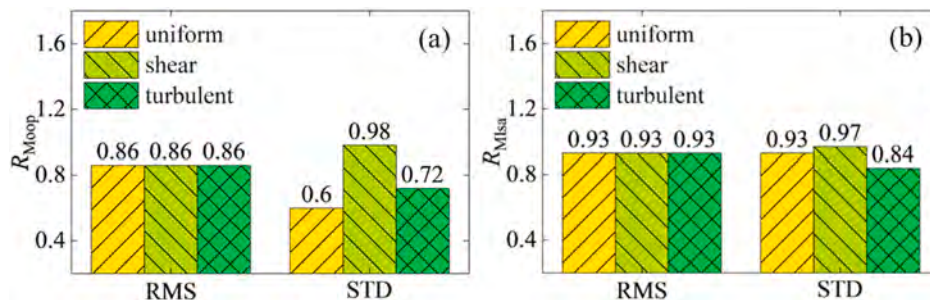
4.4.3. Wake field characteristics

The ratios of time-averaged wake field characteristics, including wake velocity (u_w) and turbulence intensity (TI), with and without considering blade deformation, are calculated using Eq. (21) and depicted in the hub-height horizontal plane ($z = 90$ m), as illustrated in Figs. 27 and 28. In these figures, white lines mark the position of the wind turbine, and black lines delineate the boundaries where $R_{uw} = 1$ and $R_{TI} = 1$.

It is observed from Fig. 27 that, under different inflow types, considering blade deformation significantly increases the wake velocity in the near wake region ($x/D < 3$) behind the wind turbine blades. In the case of uniform inflow, the increase in wake velocity caused by blade deformation extends up to $x/D = 12$. For shear inflow, the increase in wake velocity induced by blade deformation is limited to the vicinity of $x/D = 9$, while under turbulent inflow, this increase in wake velocity persists only up to $x/D = 4$.

Regarding turbulence intensity, the effect of blade deformation changes depending on the inflow condition, as shown in Fig. 28. Under uniform inflow, blade deformation increases turbulence intensity within the near wake region ($x/D < 3$), while under shear inflow, this increase in turbulence intensity due to blade deformation is confined even closer to the turbine, affecting only the region of $x/D < 1$. However, under turbulent inflow, turbulence intensity behind the wind turbine is significantly enhanced by blade deformation. Additionally, the wake vortices of the wind turbine are visualized using the Q-criterion and are

Fig. 24. Comparison results of blade root bending moments of blade #1 with and without blade deformation under different inflow conditions: (a) Out-of-plane moment M_{oop}; (b) Low-speed-axis moment M_{lsa}.
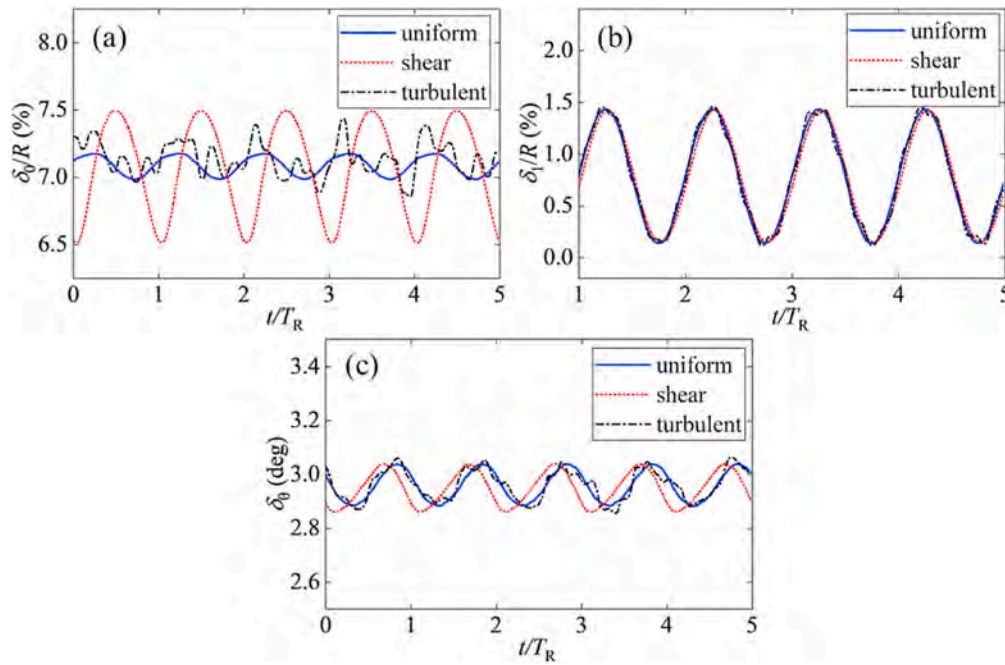
Fig. 25. Time history curves of the blade tip deformation of blade #1 under different inflow conditions: (a) Flap-wise deformation δ_0; (b) Edgewise deformation δ_1; (c) Torsional deformation δ_θ.
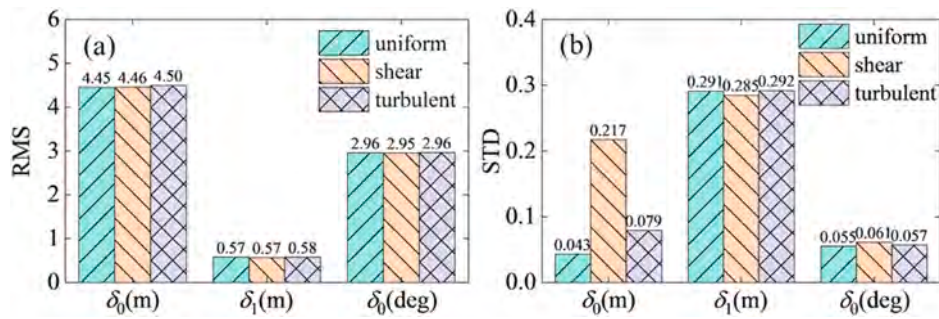
Fig. 26. Blade tip deformation of blade #1 of the wind turbine under different inflow conditions: (a) RMS; (b) STD.
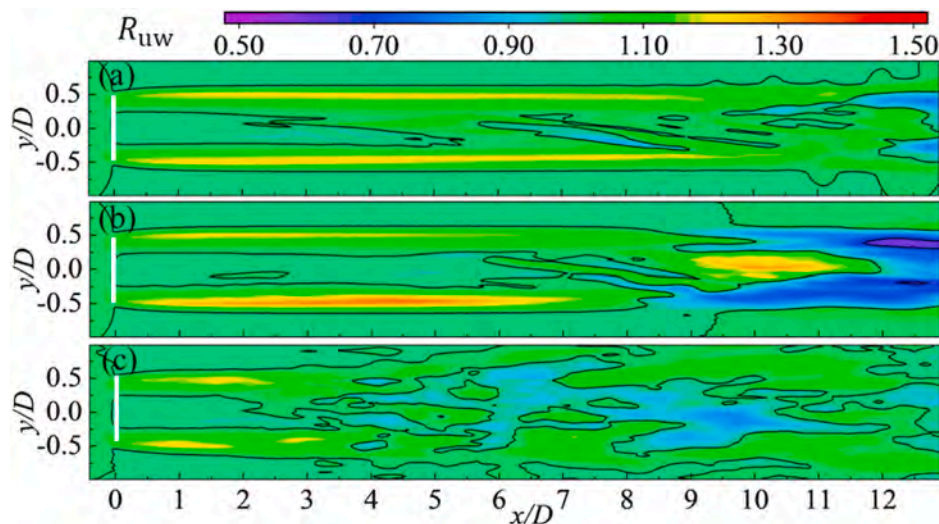
Fig. 27. Comparative analysis of wake velocity in hub-height horizontal plane ($z = 90$ m): (a) Uniform inflow; (b) Shear inflow; (c) Turbulent inflow (White line indicates the wind turbine's position).
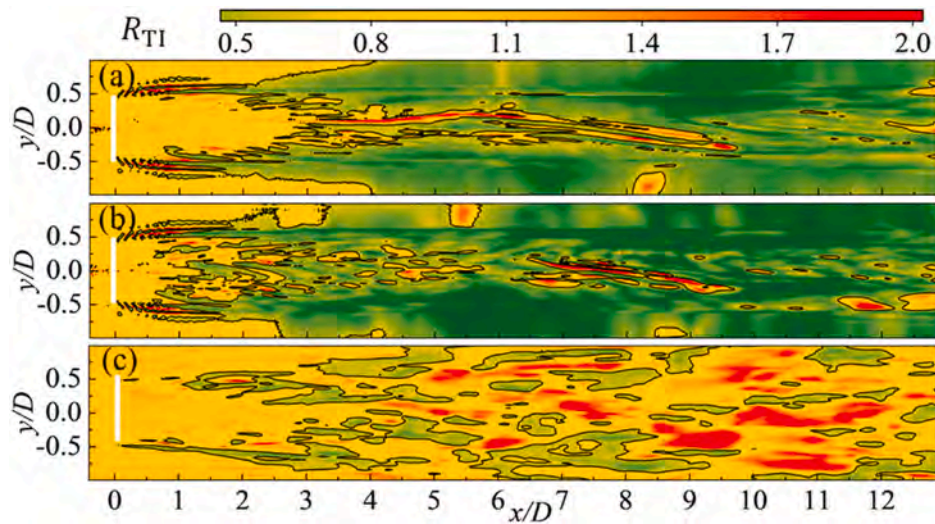
Fig. 28. Comparative analysis of turbulence intensity in hub-height horizontal plane ($z = 90$ m): (a) Uniform inflow; (b) Shear inflow; (c) Turbulent inflow (White line indicates the wind turbine's position).
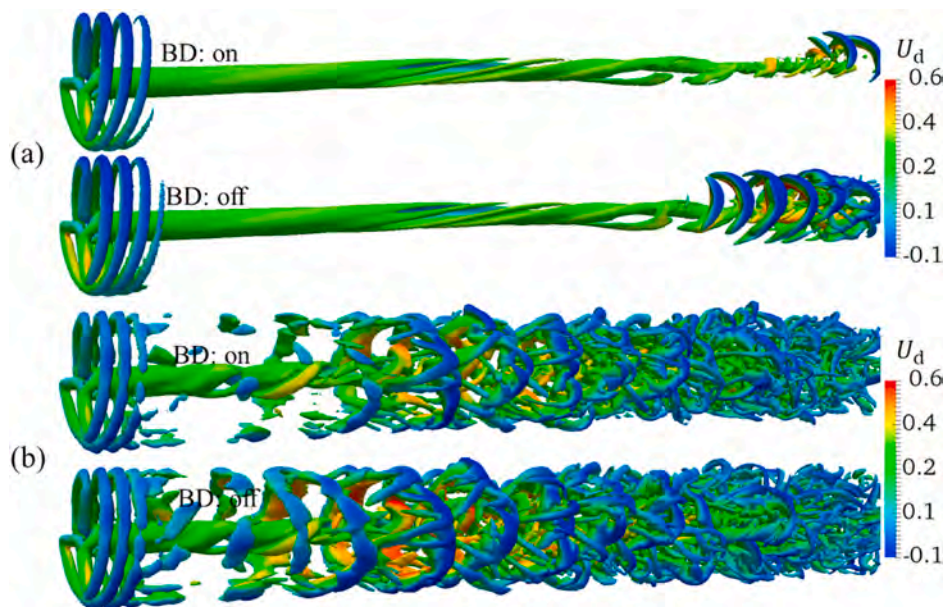
Fig. 29. Vortex structures ($Q = 5e-3$) of the wind turbine under different inflow conditions: (a) Shear inflow; (b) Turbulent inflow (BD signifies "Blade Deformation").

coloured by the dimensionless velocity deficit U_d, as presented in Fig. 29. It can be observed that the helical tip vortices shed from the blades gradually dissipate as they move downstream. As previously explained, the "disappearance" of structured wake vortices is induced by reduced Q values, resulting from the dominance of the shear component $\|\boldsymbol{S}\|^2$ over the rotational component $\|\boldsymbol{\Omega}\|^2$ in the wake flow. As the downstream distance increases and flow instability intensifies, the influence of shear forces diminishes, thereby increasing the Q value and causing sheet-like vortices to "reappear" in the far wake region. Under the turbulent inflow condition, the shear component within the wake flow is significantly weakened, consequently shortening the distance at which vortex structures "reappear".

5. Discussions

Based on the numerical results presented above, this discussion explores the aeroelastic responses of wind turbines under varied inflow conditions, emphasizing blade deformation and its impact on the aerodynamic loads and wake field characteristics at different wind speeds and inflow types.

5.1. Blade deformation under different inflow conditions

The analysis of three blade deformation types shows that flap-wise deformation has a large mean value with limited variations, whereas edgewise deformation present a small mean value but high variations. Torsional deformation notably alters the blade's AOA, thereby significantly impacting the wind turbine's aerodynamic loads. Generally, blade deformation reduces the aerodynamic loads, particularly affecting aerodynamic thrust more than aerodynamic power. Blade deformation also more profoundly affects the variation amplitude of aerodynamic loads than their mean values. As wind speed increases, mean values for all blade deformation types rise, with torsional deformation amplitude also increasing, while deformation amplitudes in both flap-wise and

edgewise decreases. Furthermore, the inflow type primarily influences the variation amplitude of flap-wise deformation, with minimal impact on the edgewise and torsional deformations.

5.2. Influence of blade deformation under various wind speed

As wind speed increases, blade deformation causes the reduction in the mean aerodynamic loads to become more pronounced. However, at lower wind speeds ($u_{in} = 5$ m/s), the impact of blade deformation on the variation amplitude of aerodynamic loads is more significant. Similarly, the reduction in the mean value of blade root bending moments due to blade deformation intensifies with increasing wind speed. Interestingly, the effect of blade deformation on the variation amplitude of M_{oop} and M_{lsa} changes with wind speed: as it rises, the reduction in the variation amplitude of M_{oop} caused by blade deformation increases, whereas that of M_{lsa} decreases. Additionally, higher inflow wind speeds extend the region of increased wake velocity caused by blade deformation further downstream, simultaneously reducing wake turbulence intensity.

5.3. Influence of blade deformation under different inflow types

Compared to uniform inflow, shear and turbulent inflow conditions significantly increase the variation amplitude of the wind turbine's aerodynamic loads, while minimally affecting their average values. Across different inflow types, blade deformation has a consistent impact on mean aerodynamic loads and blade root bending moments, with the primary differences manifesting in the variation amplitudes. Blade deformation most notably affects aerodynamic load coefficients under shear inflow and has the greatest impact on blade root bending moments under turbulent inflow. Among the different inflow conditions, the increased wake velocity region caused by blade deformation is shortest, and turbulence intensity increase is most pronounced under turbulent inflow.

6. Conclusions

In this study, an FSI model is developed by integrating an improved ALM with an equivalent beam model. Using this model in conjunction with LES, numerical simulations are then conducted on NREL 5 MW wind turbine under various inflow conditions. The aeroelastic behaviour of the wind turbine has been comprehensively analysed. From the results, the influence of blade deformation on aeroelastic responses of the wind turbine is investigated, leading to several conclusions derived from our findings.

Blade deformation leads to a decrease in the aerodynamic loads on wind turbines, a trend that becomes more pronounced with increasing wind speeds. Compared to aerodynamic power, the impact of blade deformation is more significant on aerodynamic thrust. Moreover, blade deformation has a more noticeable effect on the variation amplitude of aerodynamic loads than on their mean values. Compared to uniform inflow, shear and turbulent inflow conditions primarily increase the variation amplitude of aerodynamic loads significantly while having a small impact on their average values. The influence of blade deformation on the mean aerodynamic loads shows little change with changing inflow conditions. Furthermore, as wind speed increases, the increase in wake velocity caused by blade deformation becomes more significant, and the turbulence intensity in the wake field is lower. Compared to uniform and shear inflow conditions, under turbulent inflow, the increase in wake velocity caused by blade deformation is reduced, and it leads to an increase in turbulence intensity within the wake field.

This study enhances our understanding of how blade deformation impacts the aeroelastic performance of wind turbines at different wind speeds and under various inflow conditions. Additionally, the aeroelastic model developed holds potential for broader application in simulating and analysing large wind farms. Future research will aim to refine our knowledge of complex wake dynamics by incorporating wind farm modelling and more realistic inflow conditions, such as those from the atmospheric boundary layer.

CRediT authorship contribution statement

Yang Huang: Writing – original draft, Visualization, Validation, Software, Methodology, Investigation, Formal analysis, Data curation. **Xiaolong Yang:** Visualization, Resources, Data curation. **Weiwen Zhao:** Writing – review & editing, Software, Project administration, Investigation, Data curation. **Decheng Wan:** Writing – review & editing, Software, Resources, Methodology, Investigation, Funding acquisition, Conceptualization.

Declaration of competing interest

The authors declare that they have no known competing financial interests or personal relationships that could have appeared to influence the work reported in this paper.

Data availability

Data will be made available on request.

References

Ai, Y., Cheng, P., Wan, D., 2017. Numerical validation of aerodynamics for two in-line model wind turbines using actuator line model and CFD technique. In: International Workshop on Ship and Marine Hydrodynamics, Keelung, Taiwan, China. Nov.5-8.

Alaskari, M., Abdullah, O., Majeed, M.H., 2019. Analysis of wind turbine using QBlade software. In: IOP Conference Series: Materials Science and Engineering, vol. 518. IOP Publishing, 032020, 3.

Aryan, N., Greco, L., Testa, C., 2023. Assessment of a Fast and Versatile Aeroelastic Platform for On/off-Shore Wind Turbine Analysis.

Bazilevs, Y., Hsu, M.C., Akkerman, I., Wright, K., Takizawa, K., Henicke, B., Spielman, T., Tezduyar, T.E., 2011. 3D simulation of wind turbine rotors at full scale. Part I: Geometry modeling and aerodynamics. Int. J. Numer. Methods Fluid. 65, 207–235.

Boorsma, K., Schepers, G., Aagard Madsen, H., Pirrung, G., Sørensen, N., Bangga, G., et al., 2022. Progress in Validation of Rotor Aerodynamic Codes Using Field Data. Wind Energy Science Discussions, pp. 1–31.

Borg, M., Collu, M., Kolios, A., 2014. Offshore floating vertical axis wind turbines, dynamics modelling state of the art. Part II: mooring line and structural dynamics. Renew. Sustain. Energy Rev. 39, 1226–1234.

Bošnjaković, M., Katinić, M., Santa, R., Marić, D., 2022. Wind turbine technology trends. Appl. Sci. 12 (17), 8653.

Cai, X., Gu, R., Pan, P., Zhu, J., 2016. Unsteady aerodynamics simulation of a full-scale horizontal axis wind turbine using CFD methodology. Energy Convers. Manag. 112, 146–156.

Calabretta, A., Molica Colella, M., Greco, L., Gennaretti, M., 2016. Assessment of a comprehensive aeroelastic tool for horizontal-axis wind turbine rotor analysis. Wind Energy 19 (12), 2301–2319.

Chow, R., Van Dam, C.P., 2012. Verification of computational simulations of NREL 5 MW rotor with a focus on inboard flow separation. Wind Energy 15, 967–981.

Dai, L., Zhou, Q., Zhang, Y., Yao, S., Kang, S., Wang, X., 2017. Analysis of wind turbine blades aeroelastic performance under yaw conditions. J. Wind Eng. Ind. Aerod. 171, 273–287.

Della Posta, G., Leonardi, S., Bernardini, M., 2022. A two-way coupling method for the study of aeroelastic effects in large wind turbines. Renew. Energy 190, 971–992.

Dolan, D.S., Lehn, P.W., 2006. Simulation model of wind turbine 3p torque oscillations due to wind shear and tower shadow. IEEE Trans. Energy Convers. 21, 717–724.

Dose, B., Rahimi, H., Herráez, I., Stoevesandt, B., Peinke, J., 2018. Fluid-structure coupled computations of NREL 5 MW wind turbine by means of CFD. Renew. Energy 129, 591–605.

Duan, X., Cheng, P., Wan, D., Hu, C., 2018. Numerical simulations of wake flows of wind farm with fourteen wind turbines. In: The 28th International Ocean and Polar

Engineering Conference. International Society of Offshore and Polar Engineers, Japan. June 10-15.

Enevoldsen, P., Xydis, G., 2019. Examining the trends of 35 years growth of key wind turbine components. Energy for sustainable development 50, 18–26.

Gebhardt, C.G., Roccia, B.A., 2014. Non-linear aeroelasticity: an approach to compute the response of three-blade large-scale horizontal-axis wind turbines. Renew. Energy 66, 495–514.

Greco, L., Testa, C., 2021. Wind turbine unsteady aerodynamics and performance by a free-wake panel method. Renew. Energy 164, 444–459.

Guma, G., Bangga, G., Lutz, T., Krämer, E., 2021. Aeroelastic analysis of wind turbines under turbulent inflow conditions. Wind Energy Science 6 (1), 93–110.

Hansen, M.O.L., Sørensen, J.N., Voutsinas, S., Sørensen, N., Madsen, H.Aa, 2006. State of the art in wind turbine aerodynamics and aeroelasticity. Prog. Aero. Sci. 42, 285–330.

Hsu, M.C., Bazilevs, Y., 2012. Fluid–structure interaction modeling of wind turbines: simulating the full machine. Comput. Mech. 50, 821–833.

Huang, Y., Wan, D., Hu, C., 2021. Numerical analysis of aero-hydrodynamic responses of floating offshore wind turbine considering blade deformation. In: The 31st International Ocean and Polar Engineering Conference.

Jasak, H., Jemcov, A., Tukovic, Z., 2007. OpenFOAM: a C++ library for complex physics simulations. International workshop on coupled methods in numerical dynamics 1000, 1–20.

Jeong, M.S., Kim, S.W., Lee, I., Yoo, S.J., 2014a. Wake impacts on aerodynamic and aeroelastic behaviors of a horizontal axis wind turbine blade for sheared and turbulent flow conditions. J. Fluid Struct. 50, 66–78.

Jeong, M.S., Cha, M.C., Kim, S.W., Lee, I., Kim, T., 2014b. Effects of torsional degree of freedom, geometric nonlinearity, and gravity on aeroelastic behavior of large-scale horizontal axis wind turbine blades under varying wind speed conditions. J. Renew. Sustain. Energy 6 (2).

Jonkman, J.M., Buhl Jr, M.L., 2005. FAST User's Guide, vol. 365. Golden, CO: National Renewable Energy Laboratory, p. 366.

Jonkman, J., Butterfield, S., Musial, W., Scott, G., 2009. Definition of a 5-MW Reference Wind Turbine for Offshore System Development (No. NREL/TP-500-38060). National Renewable Energy Lab, Golden, CO USA.

Khayyer, A., Gotoh, H., Falahaty, H., Shimizu, Y., 2018. An enhanced ISPH–SPH coupled method for simulation of incompressible fluid–elastic structure interactions. Comput. Phys. Commun. 232, 139–164.

Kim, Y., Kwon, O.J., 2019. Effect of platform motion on aerodynamic performance and aeroelastic behavior of floating offshore wind turbine blades. Energies 12 (13), 2519.

Konstadinopoulos, P., Thrasher, D.F., Mook, D.T., Nayfeh, A.H., Watson, L., 1985. A vortex-lattice method for general, unsteady aerodynamics. J. Aircraft 22, 43–49.

Larsen, T.J., Madsen, H.A., Hansen, A.M., Thomsen, K., 2005. Investigations of stability effects of an offshore wind turbine using the new aeroelastic code HAWC2. In: Proceedings of Copenhagen Offshore Wind 2005, pp. 25–28. Copenhagen, Denmark.

Lee, S., Churchfield, M.J., Fleming, P., 2016. Simulator for Wind Farm Applications (SOWFA) (No. SOWFA). National Renewable Energy Laboratory (NREL), Golden, CO (United States).

Lei, H., Zhou, D., Lu, J., 2017. The impact of pitch motion of a platform on the aerodynamic performance of a floating vertical axis wind turbine. Energy 119, 369–383.

Li, Y., Castro, A.M., Sinokrot, T., Prescott, W., Carrica, P.M., 2015. Coupled multi-body dynamics and CFD for wind turbine simulation including explicit wind turbulence. Renew. Energy 76, 338–361.

Li, Z., Wen, B., Dong, X., Peng, Z., Qu, Y., Zhang, W., 2020. Aerodynamic and aeroelastic characteristics of flexible wind turbine blades under periodic unsteady inflows. J. Wind Eng. Ind. Aerod. 197, 104057.

Liu, Y., Xiao, Q., Incecik, A., 2016. Investigation of the effects of platform motion on the aerodynamics of a floating offshore wind turbine. J. Hydrodyn. 28, 95–101.

Ma, Z., Zeng, P., Lei, L.P., 2019. Analysis of the coupled aeroelastic wake behavior of wind turbine. J. Fluid Struct. 84, 466–484.

Meng, H., Lien, F.S., Li, L., 2018. Elastic actuator line modelling for wake-induced fatigue analysis of horizontal axis wind turbine blade. Renew. Energy 116, 423–437.

Micallef, D., Rezaeiha, A., 2021. Floating offshore wind turbine aerodynamics: trends and future challenges. Renew. Sustain. Energy Rev. 152, 111696.

Mikkelsen, R., 2003. Actuator Disc Methods Applied to Wind Turbines. Doctoral Dissertation. Technical University of Denmark. PhD thesis.

Musial, W.D., Beiter, P.C., Spitsen, P., Nunemaker, J., Gevorgian, V., 2018. Offshore Wind Technologies Market Report (No. NREL/TP-5000-74278; DOE/GO-102019-5192). National Renewable Energy Lab. (NREL), Golden, CO (United States), 2018.

Ning, X., Wan, D., 2019. LES study of wake meandering in different atmospheric stabilities and its effects on wind turbine aerodynamics. Sustainability 11, 6939.

Paraskeva, M., 2018. Coupled Bending-Twist Vibration of a Horizontal Axis Wind Turbine Blade Accounting for Tower Shadow under Turbulent Flow. Technical Univ. of Delft, Thesis.

Ponta, F.L., Otero, A.D., Lago, L.I., Rajan, A., 2016. Effects of rotor deformation in wind-turbine performance: the dynamic rotor deformation blade element momentum model (DRD–BEM). Renew. Energy 92, 157–170.

Qu, X., Tang, Y., Gao, Z., Li, Y., Liu, L., 2018. An analytical model of floating offshore wind turbine blades considering bending-torsion coupling effect. In: International Conference on Offshore Mechanics and Arctic Engineering, vol. 51319. American Society of Mechanical Engineers, V010T09A088.

Sayed, M., Klein, L., Lutz, T., Krämer, E., 2019a. The impact of the aerodynamic model fidelity on the aeroelastic response of a multi-megawatt wind turbine. Renew. Energy 140, 304–318.

Sayed, M., Lutz, T., Krämer, E., Shayegan, S., Wüchner, R., 2019b. Aeroelastic analysis of 10 MW wind turbine using CFD–CSD explicit FSI-coupling approach. J. Fluid Struct. 87, 354–377.

Shabana, A., 2020. Dynamics of Multibody Systems. Cambridge university press.

Shen, W.Z., Mikkelsen, R., Sørensen, J.N., Bak, C., 2005. Tip loss corrections for wind turbine computations. Wind Energy: An International Journal for Progress and Applications in Wind Power Conversion Technology 8 (4), 457–475.

Shen, W.Z., Sørensen, J.N., Zhang, J., 2007. Actuator surface model for wind turbine flow computations. European Wind Energy Conference and Exhibition.

Shourangiz-Haghighi, A., Haghnegahdar, M.A., Wang, L., Mussetta, M., Kolios, A., Lander, M., 2020. State of the art in the optimisation of wind turbine performance using CFD. Arch. Comput. Methods Eng. 27, 413–431.

Sørensen, J.N., Shen, W.Z., 2002. Numerical modeling of wind turbine wakes. J. Fluid Eng. 124, 393–399.

Sørensen, J.N., Shen, W.Z., Munduate, X., 1998. Analysis of wake states by a full-field actuator disc model. Wind Energy 1, 73–88.

Spera, D.A., 1994. Wind Turbine Technology: Fundamental Concepts of Wind Turbine Engineering, vol. 3. ASME press, New York, NY, USA.

Thomas, L., Ramachandra, M., 2018. Advanced materials for wind turbine blade-A Review. Mater. Today: Proc. 5 (1), 2635–2640.

Tran, T.T., Kim, D.H., 2016a. A CFD study into the influence of unsteady aerodynamic interference on wind turbine surge motion. Renew. Energy 90, 204–228.

Tran, T.T., Kim, D.H., 2016b. Fully coupled aero-hydrodynamic analysis of a semi-submersible FOWT using a dynamic fluid body interaction approach. Renew. Energy 92, 244–261.

Wang, L., Liu, X., Kolios, A., 2016. State of the art in the aeroelasticity of wind turbine blades: aeroelastic modelling. Renew. Sustain. Energy Rev. 64, 195–210.

Yu, D.O., Kwon, O.J., 2014. Predicting wind turbine blade loads and aeroelastic response using a coupled CFD–CSD method. Renew. Energy 70, 184–196.

Yu, Z., Zheng, X., Ma, Q., 2018. Study on actuator line modeling of two NREL 5-MW wind turbine wakes. Appl. Sci. 8, 434.

Zheng, J., Wang, N., Wan, D., Strijhak, S., 2023. Numerical investigations of coupled aeroelastic performance of wind turbines by elastic actuator line model. Appl. Energy 330, 120361.